catalysts

MDPI

Review

Recent Research Progress on Surface Modified Graphite Carbon Nitride Nanocomposites and Their Photocatalytic Applications: An Overview

Shuhan Li [1], Juntao Tan [2], Jiatong Liu [2], Yang Li [3,*], Liang Sun [4], Zhijie Huang [5] and Jiaming Li [2,*]

1 Air Force Early Warning Academy, Wuhan 430017, China; lishuhan2024@126.com
2 Guangdong Provincial Key Laboratory of Nanophotonic Functional Materials and Devices, South China Normal University, Guangzhou 510006, China; 2023022335@m.scnu.edu.cn (J.T.); 2023022441@m.scnu (J.L.)
3 College of Electrical Engineering, Naval University of Engineering, Wuhan 430033, China
4 Department of Basic Courses, Naval University of Engineering, Wuhan 430033, China; sunliang1995s@163.com
5 Wuhan National Laboratory for Optoelectronics (WNLO), Huazhong University of Science and Technology, Wuhan 430074, China; hzj@hust.edu.cn
* Correspondence: xiangyangliyang@foxmail.com (Y.L.); jmli@m.scnu.edu.cn (J.L.)

Abstract: Semiconductors with visible light catalytic characteristics can realize the degradation of pollutants, CO_2 reduction, and hydrogen preparation in sunlight. They have huge application value in the fields of environmental repair and green energy. Graphite phase nitride (g-C_3N_4, CN) is widely used in various fields such as photocatalytic degradation of pollutants due to its suitable gap width, easy preparation, low cost, fast visible light response, and rich surface activity sites. However, the absorption rate of ordinary CN on visible light is low, and the carriers are easy to recombination, making the lower optical catalytic activity. Therefore, in order to improve the photocatalytic characteristics of the CN, it is necessary to make the surface modification. This article first introduces several main methods for the current surface modification of CN, including size regulation, catalyst embedding, defect introduction, heterostructure construction, etc., and then summarizes the optical catalytic application and related mechanisms of CN. Finally, some challenges and development prospects of CN in preparation and photocatalytic applications are proposed.

Keywords: graphite phase carbon nitride; surface modification; photocatalytic

Citation: Li, S.; Tan, J.; Liu, J.; Li, Y.; Sun, L.; Huang, Z.; Li, J. Recent Research Progress on Surface Modified Graphite Carbon Nitride Nanocomposites and Their Photocatalytic Applications: An Overview. *Catalysts* **2024**, *14*, 636. https://doi.org/10.3390/catal14090636

Academic Editor: Jorge Bedia

Received: 31 August 2024
Revised: 14 September 2024
Accepted: 16 September 2024
Published: 19 September 2024

1. Introduction

With the rapid development of the industry, the problems of energy shortage, environmental pollution, and climate warming are becoming more and more serious. The semiconductor-based photocatalytic materials are considered to be an effective solution to address energy shortages, improve environmental problems, and promote social and economic sustainable development. This is because driven by the semiconductor, the solar energy can be directly converted into precious chemical fuel, such as hydrogen and its compounds, thereby alleviating the shortage of energy. At the same time, semiconductors can also use solar energy to degrade organic pollutants, such as antibiotics and dyes to govern environmental pollution. In addition, semiconductors can also reduce CO_2 to CO, CH_4, methanol, ethanol, and other products in the solar environment, thereby providing high-value chemical industrial products while alleviating the effect of greenhouses [1–7]. In the past two decades, various types of metal oxide semiconductor materials (such as CdS, TiO_2, ZnO, etc.) have been used in the photocatalytic fields [8–11]. However, due to the wider gaps of metal oxides, the utilization rate of solar light is too low, which limits the application of this type of photocatalytic material. Although the band width of metal sulfides is more friendly to the use of sunlight, metal sulfides will cause light corrosion and self-oxidation under the condition of light, and the chemical properties are unstable. Thus,

researchers have always hoped to find a photocatalytic material with strong optical activity and stable chemical properties.

As early as 1996, Teter et al. found that the carbon nitride had five objects with the structure of a-phase, cubic phase, quasi-cubic phase, and graphite phase through calculations, of which the graphite phase was the most stable [12]. In 2009, Wang et al. successfully applied graphite phase nitride (g-C_3N_4, CN) to photocatalytic hydrogen-made hydrogen, creating a new era of CN applied in photocatalytic [13]. Since then, the research on CN has quickly become a very popular research hotspot, and a large amount of research on CN has been reported. CN is a typical N-type non-metallic semiconductor material with a graphite-like layered structure, rich in carbon, nitrogen, and hydrogen. The gap of the CN is about 2.7 eV and the absorption spectrum is mainly in the visible light range of 400–460 nm. It is easy to prepare, non-toxic, has strong optical chemical stability, and has well-equipped structure matching, thus it is widely used in photocatalytic decomposition of hydrogen, photocatalytic organic pollutants degradation, and photocatalytic CO_2 reduction [14–17]. Generally speaking, CN can be prepared by thermal polymerization (including water thermal heat, melting salt method, etc.) through thermal polymerization including urea, cyanamide, melamine, and thiourea. This method is simple to prepare and conducive to large-scale production. Among them, the method of thermally condensing cyanamide to form dicyandiamide, then further condensing it into melamine, and finally gradually condensing melamine into CN is considered an efficient method for producing relatively few defects [18]. However, the CN prepared by the traditional thermal aggregation has a smaller surface area, many defects, and the recombination rate of photoinduced electrons and holes is high, which seriously restricts its photocatalytic activity [19]. In order to improve the problems of CN such as many defects and easy recombination of carriers, researchers have completed a lot of work on the surface modification of CN in recent years and achieved the efficient photocatalytic application of CN through morphology control, defect engineering, element doping, heterostructure construction, etc. [20–23].

So far, there is much research on the progress of the preparation of CN and its applications in various fields, including a review of the latest research on the preparation of crystalline CN and its application in the field of photocatalytic [24–27]. While this paper focuses on the latest research progress of CN, especially in the surface modification method such as size regulation, elemental doping, defect regulation, heterogeneous construction, and new catalyst design for enhanced photocatalytic performance. Additionally, this paper also systematically summarizes the applications of CN in the field of optical catalysts, especially in the optical degradation of heavy metals and organic pollutants, photocatalytic decomposition of H_2O to produce hydrogen, photocatalytic CO_2 reduction, and optical catalytic preparation of the H_2O_2 and the corresponding mechanism of photocatalytic was discussed combined with the performance changes after CN modification. Finally, the current challenges, future development trends, and prospects faced by CN semiconductor materials in the field of optical catalytics are discussed.

2. Research Progress on Surface Modification of CN

2.1. Size Regulation

Although CN is considered an excellent photocatalytic material, the CN prepared by traditional methods often has problems such as large size and smaller surface area, which limits the exposure of its active site and affects catalytic performance. The size regulation of CN can increase the specific surface area, optimize the energy band structure, and expose more active sites, which can broaden the absorption range of visible light, facilitate the migration of electrons in the photocatalytic process, and improve photocatalytic efficiency. Therefore, the size regulation of CN is an important way to achieve an excellent photocatalytic effect [28].

2.1.1. Two-Dimensional (2D) CN Nanosheets

In general, CN nanosheet structure cannot be produced by directly calcining a precursor solution containing CN, and a secondary annealing was required. Shen et al. used urea as a precursor, first calcined at 550 °C in a muffle furnace for 4 h, and then annealed at 500 °C for 2 h to obtain CN nanosheets [29]. Similarly, Shi et al. used dicyandiamide as a precursor, first calcined at 550 °C in a muffle furnace for 4 h, and then calcined again at 510 °C for 2 h, finally obtaining CN nanosheets [30]. Wang et al. utilized the bottom-up green acidification method to prepare the ultra-thin CN nanosheets. As shown in Figure 1A–E, the precursor was obtained by mixing melamine and diluted sulfuric acid solution and then undergoing hydrothermal treatment which was calcined in a muffle furnace at 550 °C for 4 h. The CN nanosheets treated with sulfuric acid hydrothermal have a larger specific surface area and more obvious 2D-layered characteristics than the CN nanosheets treated with acid alone [31]. Similarly, Amir et al. first calcined melamine in a crucible at 520 °C for 5 h to form bulk CN (BCN) through thermal polycondensation. Then, the bulk CN is mixed with sulfuric acid, and the sulfuric acid is stirred to penetrate and act on the interlayers of CN, destroying the van der Waals force between the layers, thereby achieving the exfoliation of CN and forming a suspension of CN. The suspension was then washed repeatedly with deionized water and ethanol and then dried in a vacuum drying oven at 60 °C to obtain preliminary purified CN nanosheets. To further increase the porosity of CN nanosheets, the dried powder was heated at 400 °C for 1 h. The resulting CN nanosheets had a large specific surface area and catalytic activity [32,33].

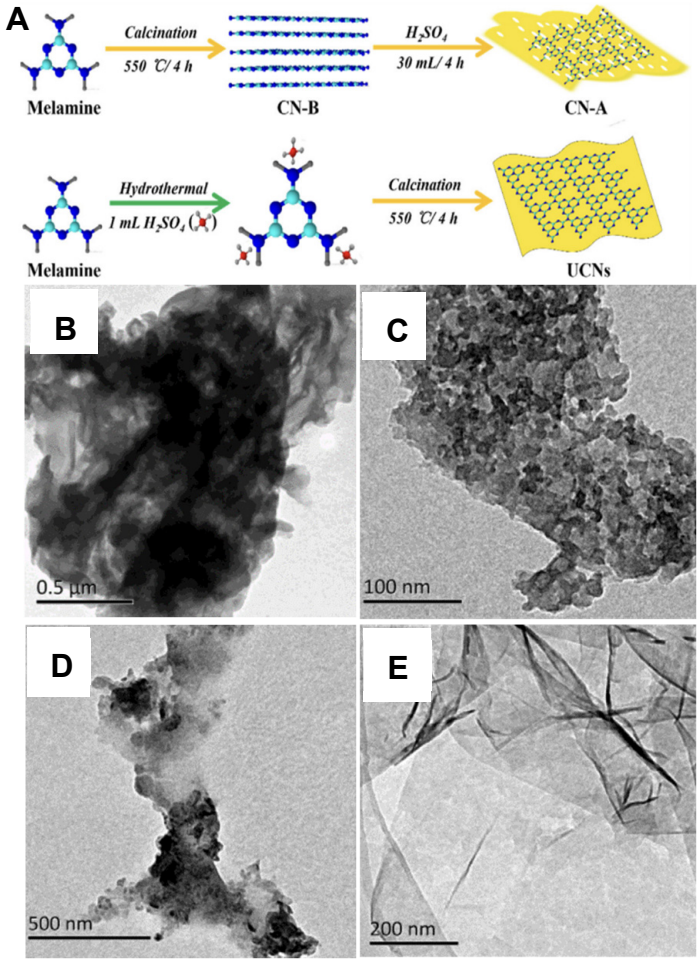

Figure 1. (**A**) Synthesis Procedure of Nanosheets of CN; TEM images of (**B**) bulk CN; (**C**) acid-treated CN; (**D**) hydrothermal treatment of melamine without acid and (**E**) Ultrathin CN nanosheets [31]. Reprinted with permission from Ref. [31].

In addition to the calcination method, the liquid-phase exfoliation method can also obtain CN nanosheets. Masih et al. put the anterior urea in the furnace at 550 °C for 4 h with a calcination method, and then disperse the obtained BCN in the ion water for 4 h ultrasonication. The BCN was removed, and then the upper liquid was dried to receive the CN nanosheets [34]. Furthermore, Yi et al. used the NB_2O_5-mediated thinning strategy to prepare a large amount of CN nanosheets, the interlayer distance of the nanosheets was significantly shortened, which was more conducive to electron transmission and thus improved photocatalytic efficiency [35].

Ma et al. developed a simple method to anchor CN quantum dots (CNQDs) onto CN nanosheets to form a homojunction structure (HJ-CN), which could improve photocatalytic performance largely without introducing metal elements [36].

2.1.2. One-Dimensional (1D) CN Nanotubes and Nanorods

In recent years, the preparation and photocatalytic research of 1D CN nanotubes and nanorods have also been widely reported. Due to their shortened radial width and elongated axial length, the photoelectric properties of 1D CN nanomaterials can be well adjusted by controlling their size.

Guo et al. used hexagonal rod-shaped single-crystal supramolecules as precursors to prepare hexagonal P-doped CN nanotubes with a layered structure. Experimental results show that compared with ordinary CN, hexagonal CN nanotubes have more active sites and their specific surface area is significantly increased. At the same time, due to the doping of P, the band gap becomes narrower, the conductivity is improved, and the hydrogen evolution efficiency has also increased [37]. Liu et al. heated a mixture of $NaH_2PO_4 \cdot H_2O$ and melamine at a high temperature and achieved large-scale rapid synthesis of P-doped CN nanotubes. During the synthesis process, $NaH_2PO_4 \cdot H_2O$ generates phosphine gas at high temperatures, which induces the transformation of CN from 2D nanosheets to 1D nanotubes [38]. Li et al. prepared modified CN nanotubes by a two-step hydrothermal-thermal polycondensation method using a combination system of urea and melamine as precursors. The experiments show that controlling the reaction temperature can effectively adjust the vacancy concentration on the nanotubes, and a larger vacancy concentration is conducive to capturing photogenerated electrons. In addition, the tubular structure makes the transmission path of electrons from the bulk phase to the surface phase shorter, and the photocatalytic activity is greatly improved [39]. Before preparing CN nanotubes, Zhang et al. first placed melamine in a NaOH aqueous solution for hydrothermal pretreatment, then calcined the pretreated product, and finally obtained CN nanotubes. The studies show that the production of CN nanotubes is attributed to the hydrothermal pretreatment process because cyanuric acid is generated in this process, which will form a supramolecular precursor through self-assembly with melamine. The precursor can be calcined to form CN nanotubes, which have excellent photocatalytic hydrogen evolution properties [40]. Guo et al. prepared CN nanotubes with abundant nitrogen-vacancy defects by a simple sodium borohydride thermal reduction method. As shown in Figure 2A, a mixture of melamine and urea was first calcined under an inert gas N_2 to prepare CN nanotubes, which were then mixed with sodium borohydride and further calcined under N_2 to obtain defect-rich porous CN nanotubes. As shown in Figure 2B–E, Scanning Electron Microscope (SEM) and transmission Electron Microscope (TEM) images show that the porous CN nanotubes have a uniformly distributed porous hollow tubular structure with a diameter of about 200 nm and a wall thickness of about 26 nm. The porous hollow structure can provide abundant surface active sites, which is beneficial to improving the photocatalytic performance [41].

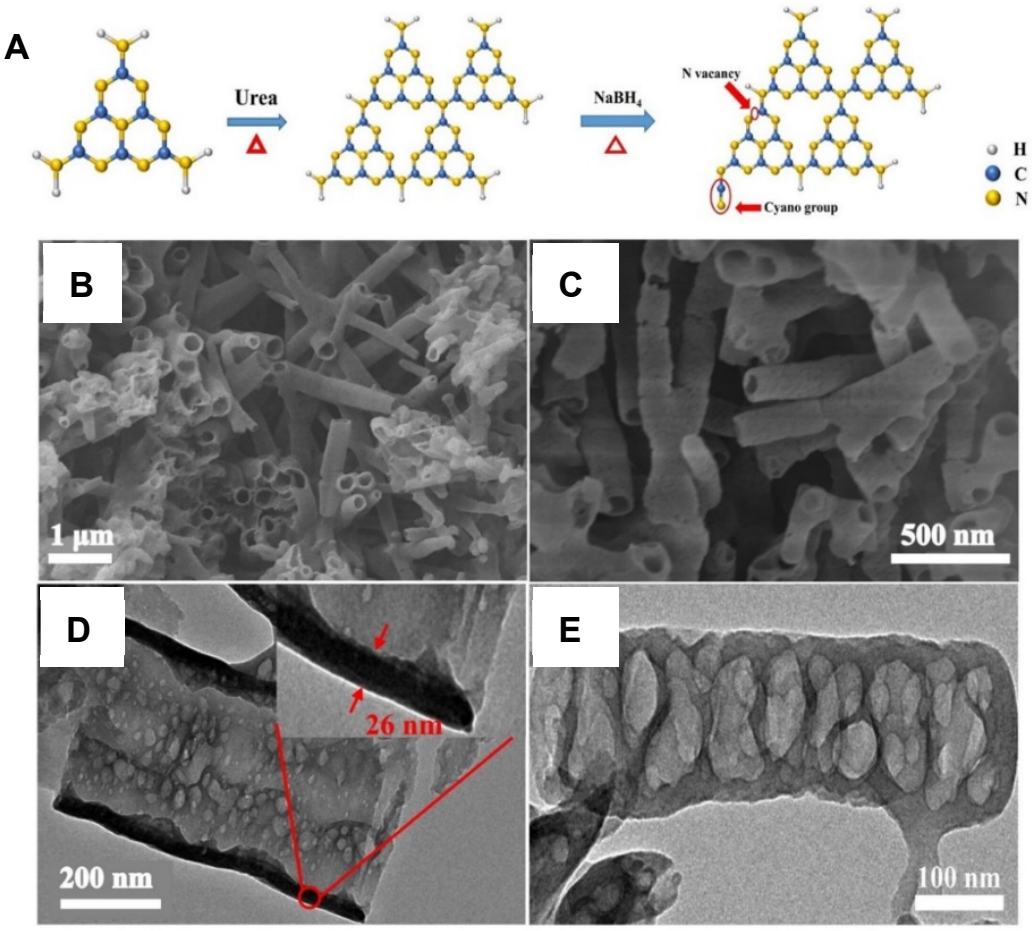

Figure 2. (**A**) Scheme for the formation of DTCN; (**B**,**C**) scanning electron microscope; (**D**,**E**) transmission electron microscope images of TCN and DTCN (inset: high magnification image). DTCN, defective porous CN nanotube [41]. Reprinted with permission from Ref. [41].

Preeyanghaa et al. used melamine and $HONH_2$.HCl complex as templates to synthesize hierarchical CN nanorods with carbon vacancies by ultrasonic-assisted thermal polycondensation. The nanorods can promote light scattering, have a large specific surface area and active sites, and provide abundant transport channels for charge migration. In addition, the presence of carbon vacancies can also serve as shallow charge capture centers and promote charge separation [42]. Zou et al. can universally prepare 1D porous CN nanorods containing nitrogen vacancies and oxygen doping with a variety of nitrogen-containing precursors through the hydrogen bonding structure and molecular shearing effect of "nitrogen-containing precursor-nanocellulose". As shown in Figure 3A, the preparation process of CN-based photocatalyst mainly includes the hydrogen bonding between dicyandiamide and the functional groups of nanocellulose-hydroxyl and carboxyl groups, and the subsequent thermal polymerization and H_2O_2 molecular shearing process. The morphology of CN nanorods is shown in Figure 3B–I, in the preparation process of the above catalyst, nanocellulose plays the role of soft template and dopant at the same time. Therefore, nitrogen vacancies and oxygen doping were successfully introduced into the molecular skeleton of CN. Under the molecular shearing action of H_2O_2, CN was converted into one-dimensional nanorods, and the nanorods were filled with nanosheet frameworks. The 1D nanorod-like structure greatly increased the specific surface area of CN, exposed a large number of active sites, and enhanced the photocatalytic activity [43]. Liang et al. first heated melamine in the crucible at 500 °C for 4 h, and then put it in a tube furnace with KCl and LiCl, heated at 550 °C in the N_2 atmosphere for 4 h. The obtained products were washed with boiling water. Finally, after drying at 60 °C for one night, CN nanorods

were obtained. Subsequently, W-doped highly crystalline CN nanorods catalysts were successfully prepared by a solvothermal-assisted W-doping method for photocatalytic CO_2 reduction [44].

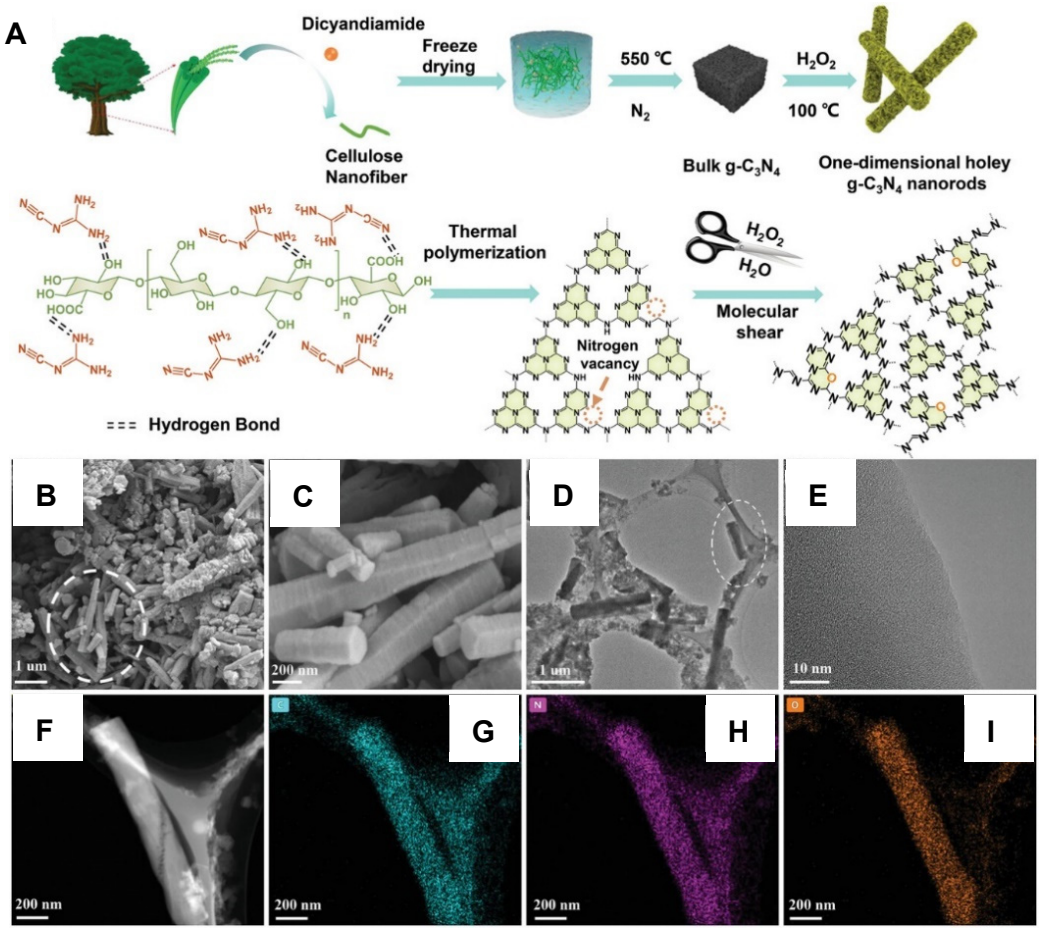

Figure 3. (**A**) Illustration of the synthetic route and chemical structure of the nitrogen deficient HCN with oxygen doping; (**B**,**C**) SEM; (**D**–**F**) TEM images of HCN-0.01 and (**G**–**I**) the corresponding elemental mapping on C, N, and O [43]. Reprinted with permission from Ref. [43].

2.1.3. Zero-Dimensional (0D) CN Quantum Dots (QDs)

In recent years, in addition to the research on 2D and 1D CN nanomaterials, researchers have also reported the synthesis methods of 0D CNQDs. As the size becomes smaller, CN exhibits a larger specific surface area and more surface active sites. As usual, 0D QDs can be prepared by hydrothermal method, solvothermal method, solid phase method, etc. Their unique quantum confinement effect and optical properties can enhance light absorption, thereby improving photocatalytic performance. He et al. first synthesized BCN by heating melamine in air and N_2 atmosphere through a thermal polycondensation method and then placed the BCN in water or ethanol solution for ultrasonic exfoliation for about 16 h to prepare 0D CNQDs at room temperature [45]. Hong et al. prepared B-doped CN using a mixture of boric acid, melamine, and urea as a precursor and then put it in the potassium hydroxide (KOH) ethanol solution through the water heat method to obtain the B-doped CNQDs. The preparation process and morphological characterization results are shown in Figure 4A–E. The morphological tests show that the size of CNQDs is about 1.5 nm. They are finally loaded onto $Ni(OH)_2$ nanoflowers to form $Ni(OH)_2$ nanoflowers doped with B-doped CNQDs [46].

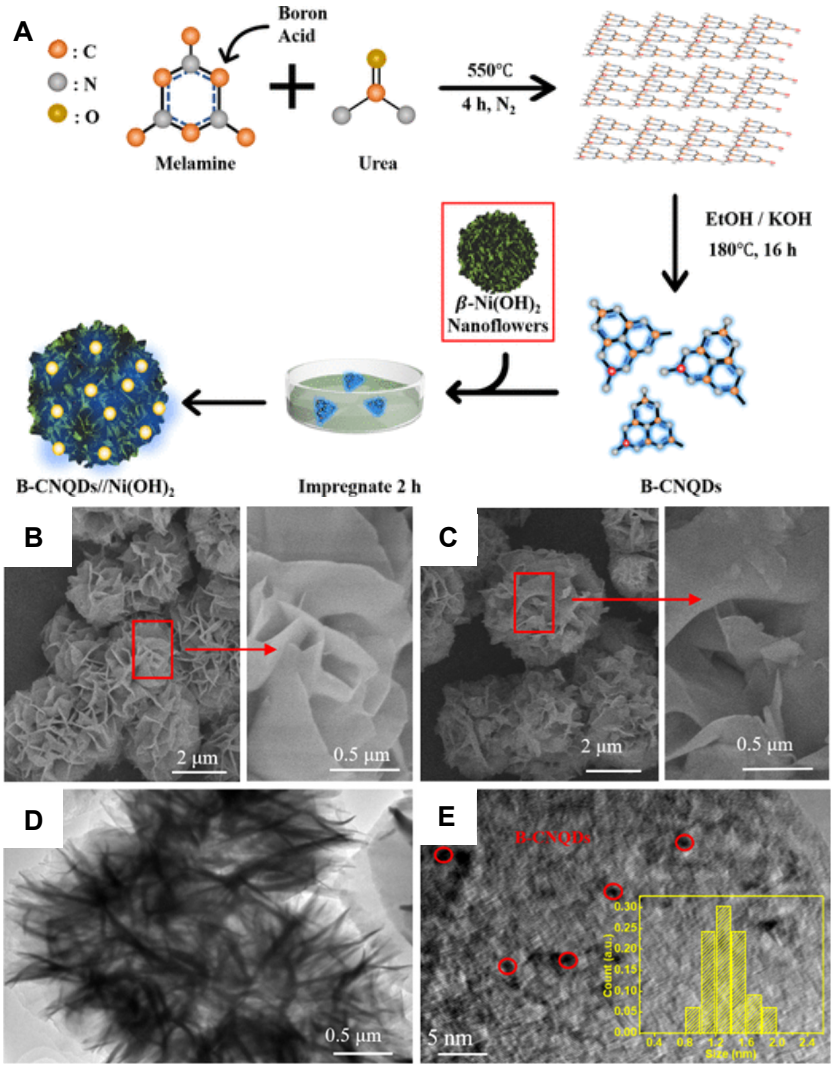

Figure 4. (**A**) Diagram illustration for the synthesis of B-CNQD$_X$-Ni nanoflowers; (**B**) SEM images of Ni(OH)$_2$ nanoflowers; (**C**) SEM images of B-CNQD$_{10}$-Ni nanocomposites, and (**D**) TEM and (**E**) HRTEM images of B-CNQD$_{10}$-Ni nanocomposites [46]. Reprinted with permission from Ref. [46].

Dai et al. first prepared sulfur-doped BCN, and then used S-doped CN as a precursor and ultrasonically exfoliated the S-doped CN to obtain S-doped CNQDs. Studies on its fluorescence properties have shown that the average size of S-doped CNQDs is 2 nm and has an emission peak at 460 nm, covering the luminescence spectrum region of 550 nm, proving that the band gap of CNQDs has been adjusted and the light absorption range has been significantly increased [47]. Ma et al. ground the mixture of melamine and sodium citrate, added the resulting powder into ultrapure water, and then transferred it to a reactor and heated it at 180 °C for 2 h. After natural cooling, the obtained solution was dialyzed in pure water for 48 h, and the dialysate was freeze-dried to obtain CNQDs. Subsequently, CNQDs were introduced into the prepared planar structured CN, which broadened the light absorption range of the photocatalyst, promoted the separation of photogenerated carriers, and increased the specific surface area of the catalyst, thereby providing more active sites and effectively improving the performance of photocatalytic hydrogen evolution [48]. Similarly, Eroglu et al. fabricated a novel ternary heterojunction photocatalyst by decorating reduced graphene oxide/black phosphorus binary heterojunctions (rGOBP) with carbon CNQDs via the ultrasound-assisted liquid exfoliation method for an enhanced photocatalytic performance [49]. Finally, the comparison table of the most active photocatalysts is listed in Table 1.

Table 1. The size regulation of CN for photocatalytic.

Material Type	Synthesis Method	Photocatalytic System	Reference
2D CN nanosheets	Calcining + Annealing	H_2 production	[29]
2D CN nanosheets	Calcining + Annealing	CO_2 reduction	[30]
2D ultra-thin CN nanosheets	Acid + Hydrothermal + Calcining	H_2 production	[31]
2D CN nanosheets	Calcining + Acid + Annealing	H_2 production	[32]
2D CN nanosheets	Calcining + Acid + Annealing	H_2 production	[33]
2D CN nanosheets	liquid-phase exfoliation	H_2 production	[34]
2D CN nanosheets	NB_2O_5-mediated thinning strategy	H_2 production	[35]
2D CN nanosheets	Hydrothermal	H_2 production	[36]
1D P-doped CN nanotubes	Hydrothermal	H_2 production	[37]
1D P-doped CN nanotubes	Hydrothermal	CO_2 reduction	[38]
1D CN nanotubes	Hydrothermal	NO reduction	[39]
1D CN nanotubes	Hydrothermal	H_2 production	[40]
1D N-defect CN nanotubes	sodium borohydride thermal reduction	H_2 production	[41]
1D C-defect CN nanorods	ultrasonic-assisted thermal polycondensation	Tetracycline degradation	[42]
1D N/O-defect CN nanorods	Hydrothermal	H_2 production	[43]
1D C-doped CN nanorods	solvothermal-assisted	CO_2 reduction	[44]
0D CNQDs	N_2-assisted thermal polycondensation	QLED displays	[45]
0D B-doped CNQDs	Hydrothermal	Supercapacitors	[46]
0D S-doped CNQDs	Hydrothermal + Ultrasonic	Bioimaging	[47]
0D CNQDs	Ground + Hydrothermal	H_2 production	[48]
rGOBP/0D CNQDs	Ultrasound-assisted liquid exfoliation	Methyl orange degradation	[49]

2.2. Defect Control

The introduction of defects in CN is a research hotspot in defect regulation. Research has shown that the introduction of point defects in CN is widely studied, and CN point defects include vacancy defects of carbon vacancies and nitrogen vacancies, as well as anti-site defects of carbon and nitrogen self-doping.

Based on density functional theory (DFT), Zhang et al. calculated the optimal structures and excited states of intrinsic CN and defective CN. The research results show that the absorption spectrum of defective CN has a red shift, and the absorption intensity of visible light is significantly improved, especially for the defective CN structure with superior carbon atom defects. Further research also found that vacancy defects have a negative impact on CN. Charge transfer and excited state electron-hole distribution will have an impact, and as defects appear, the charge migration distance will also increase [50]. Ma et al. mixed melamine and NaN_3 and prepared porous CN rich in N defects in an Ar atmosphere. The results show that the introduction of N defects into CN can significantly reduce the bandgap width and inhibit the recombination of electrons and holes. Thereby improving the reduction efficiency of CO_2 [51]. Lv et al. used melamine as a precursor and prepared porous CN rich in N defects by secondary calcination in an Ar atmosphere. Further calculations using DFT show that N_2 molecules are more easily adsorbed on the nitrogen vacancies of porous CN, as shown in Figure 5A–C [52]. Liu et al. prepared porous defective CN nanosheets by thermal condensation of freeze-dried precursors. They also used DFT to predict the application of these defective nanosheets in regulating photocatalytic performance. The study shows that CN nanosheets containing defects have more active sites and can enhance visible light absorption capacity [53]. Luo et al. used nitrogen deficiency carbon nitride as a model catalyst and proposed several different reaction mechanisms of photocatalytic H_2O_2 production, proving that H_2O_2 can be generated through multiple pathways and highlighting the main roles of $^1O_2$, which are ignored by previous studies [54]. Shiraishi et al. prepared mesoporous CN (GCN) catalysts with different surface areas by silica-templated thermal polymerization of cyanamide and studied the effects of surface defects on photocatalytic H_2O_2. The defects on mesoporous GCN can behave as the active sites for four-electron reduction of O_2, thus decreasing the H_2O_2 selectivity. While the GCN catalysts with relatively large surface area but with a small number of surface

defects can promote relatively efficient H_2O_2 formation [55]. Xie et al. introduced two types of cooperative N vacancies, NH_x and N_{2C} vacancy, into the framework of polymeric carbon nitride and found that the optimized sample delivers a 15 times enhancement in solar-driven H_2O_2 production as well as excellent stability [56]. Finally, the comparison table of the most active photocatalysts is listed in Table 2.

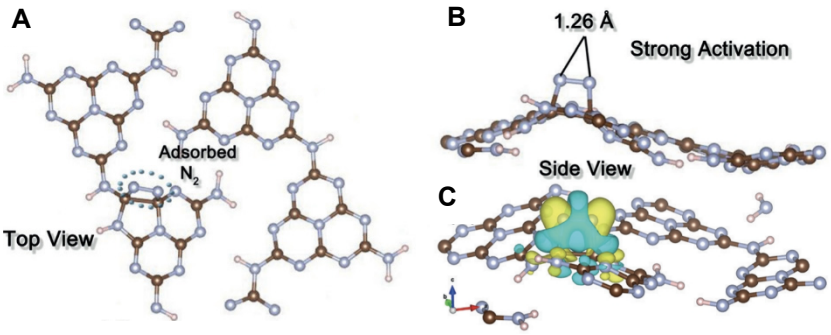

Figure 5. (**A**) N_2 adsorption geometry on polymeric carbon nitride with nitrogen vacancy; (**B**) and (**C**) The charge density difference of the N_2-adsorbed polymeric carbon nitride with nitrogen vacancy; the yellow and blue isosurfaces represent charge accumulation and depletion in the space, respectively [52]. Reprinted with permission from Ref. [52].

Table 2. The defect control of CN for photocatalytic.

Material Type	Synthesis Method	Photocatalytic System	Reference
C/N defects-CN	DFT calculation	All photocatalytic system	[50]
N defects-CN	Hydrothermal	CO_2 reduction	[51]
N defects-CN	Hydrothermal	N_2 reduction	[52]
N defects-CN	Hydrothermal	Bacteria sterilization	[53]
N defects-CN	Hydrothermal	H_2O_2 production	[54]
Amine moieties-CN	Hydrothermal	H_2O_2 production	[55]
N defects-CN	Hydrothermal	H_2O_2 production	[56]

2.3. Element Doping

As mentioned above, the bandgap width of CN is generally around 2.7 eV, and it can absorb visible light with a wavelength of less than 460 nm. Element doping can effectively adjust the bandgap width of CN, enhance light absorption, and thus optimize photocatalytic performance. Hong et al. used melamine as a precursor solution and prepared B-doped CN nanotubes by calcination and hydrothermal method. Studies have shown that after the incorporation of B, new impurity energy levels are generated inside the CN nanotubes, increasing the number of active sites and effectively promoting the separation of photogenerated electrons and holes, ultimately improving the efficiency of photocatalytic hydrogen evolution [57]. Huang et al. treated melamine with different acids such as sulfuric acid and nitric acid to obtain CN materials containing various oxygen functional groups. Studies have shown that although the doping of nitrogen-carbon-oxygen (N-C-O) and carbon-oxygen-carbon (C-O-C) can effectively hinder the recombination of photogenerated electrons and holes in CN and improve photocatalytic performance, the effects of these two groups on the photocatalytic performance of CN are completely different. The electron-withdrawing effect of C-O-C firmly holds the electrons. Although it promotes the separation of photogenerated electrons and holes and prolongs the electron life, it is difficult for the electrons to migrate out of the triazine ring, and its photocatalytic hydrogen production performance is inhibited. The N-C-O group forms a bridge connecting the triazine structures within the CN molecule, allowing electrons to move between different triazine structures. This not only promotes the separation of photogenerated electrons and holes but also promotes the transfer of electrons between

triazine structures, making the N-C-O-doped CN have higher photocatalytic hydrogen production performance [58]. Dang et al. embedded P, N co-doped carbon nanomaterials in CN hollow spheres, and designed and constructed a photocatalytic nanoreactor system. P, N co-doped carbon nanomaterials serve as active sites, which can become acceptors of photogenerated electrons and accelerate the separation of photogenerated electrons and holes, greatly improving the production rate of H_2O_2 [59]. Sun et al. prepared F-doped porous CN by directly calcining melamine in an F-containing atmosphere. The study shows that the right calcination temperature is the key to preparing good photocatalysts. The morphology and photocatalytic activity of CN can be controlled by controlling the fluorination temperature. When the fluorination temperature increases, the pores of CN will gradually become larger. At 180 °C, the porous structure of CN will seriously deteriorate and the thickness will become thinner. When the fluorination temperature is 150 °C, the hydrogen evolution efficiency of CN is the highest [60]. Zhang et al. fabricated a nitrogen vacancy-modified B-doped CN photocatalyst with high efficiency of H_2O_2 production without adding a scavenger based on ion-doping and defect construction, and the system produced H_2O_2 in-situ through photocatalytic action and promoted the Fe^{2+}/Fe^{3+} cycle under the action of photo-generated electrons [61]. Wang et al. employed an innovative strategy to investigate the relationship between the H-containing structures of CN and its water-splitting properties, and the newly synthesized CN sample demonstrates an enhanced H_2 yield by a factor of 17 compared to that of pure CN [62].

In addition to non-metallic doping, research on metal and metal/non-metallic doping is also extensive. Shi et al. prepared Co/Fe bimetallic doped CN with N defects using a simple salt template method. Experiments show that when the Fe/Co ratio is 2.5: 2.5, the prepared doped catalyst has the best photo-Fenton-like catalytic performance and can effectively degrade organic wastewater [63]. Jiang et al. prepared CN doped with alkali metals Li, Na, and K by a high-temperature assisted method. The band gap width of CN is improved, the number of surface active sites is increased, the specific surface area is increased, and the catalytic hydrogen evolution performance under visible light is greatly improved. Among the three alkali metal ion-doped CN, Na-doped CN has the best bandgap and the highest photocatalytic activity [64]. Ma et al. prepared Fe/CN material by one-step thermal polymerization using ferric nitrate nonahydrate and melamine as precursors. Research has shown that Fe can be doped into CN in a suitable state without changing the layered structure, and can also coordinate with nitrogen atoms to form embedded compounds, thereby regulating the energy band structure and improving the absorption rate of photocatalytic materials to visible light [65]. Xu et al. proposed a salt template-induced homogeneous doping strategy and synthesized a new type of carbon/P-doped red polymerized CN using a dopant similar to melamine. As shown in Figure 6A–E, compared with traditional CN and other red carbon-based photocatalysts, this material has a narrower band gap (1.71 eV) and stronger near-infrared absorbance ($\lambda > 700$ nm), achieving efficient near-infrared photocatalytic hydrogen production and the highest apparent quantum efficiency [66].

As a special type of material among metals, noble metals have received extensive attention and research due to their strong localized surface plasmon effect (LSPR). Since the band gap of CN is generally around 2.7 eV and the maximum absorption wavelength is about 460 nm, it is unable to effectively utilize long-wavelength visible light, which limits the photocatalytic efficiency of CN [67]. The use of noble metal loading can improve the visible light response range of CN. Yi et al. loaded Ag onto CN to prepare modified Ag-doped CN, whose LSPR excitation peak is between 450–500 nm, and the light response range is improved compared with ordinary CN [68]. Zhao et al. prepared an Au-doped CN/Co_3O_4 plasma heterojunction photocatalyst. As shown in Figure 7A–I, the TEM morphology shows that Au is loaded on CN, and finally both are loaded on Co_3O_4 to form a Z-type heterojunction. This design applied the Au plasma effect and Z-type charge transfer mechanism to broaden the response range of the photocatalyst. The corresponding LSPR excitation peak was between 500 and 600 nm, which effectively enhanced the performance of photocatalytic degradation of organic pollutants such as bisphenol A [69].

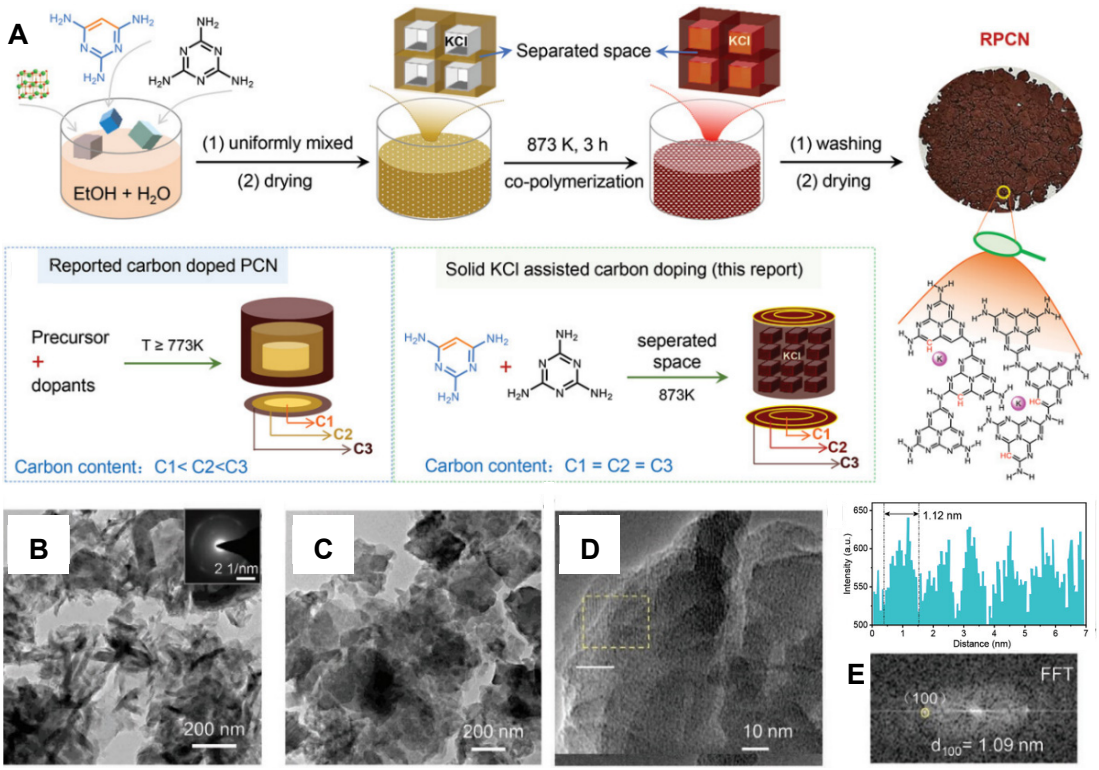

Figure 6. (**A**) Schematic illustration of salt-template-induced homogeneous incorporation strategy; TEM images of (**B**) polymeric carbon nitride, (**C**,**D**) red polymeric carbon nitride; (**E**) The Fast Fourier Transform (FFT) pattern of red polymeric CN corresponding to the yellow framework of (**D**) [66]. Reprinted with permission from Ref. [66].

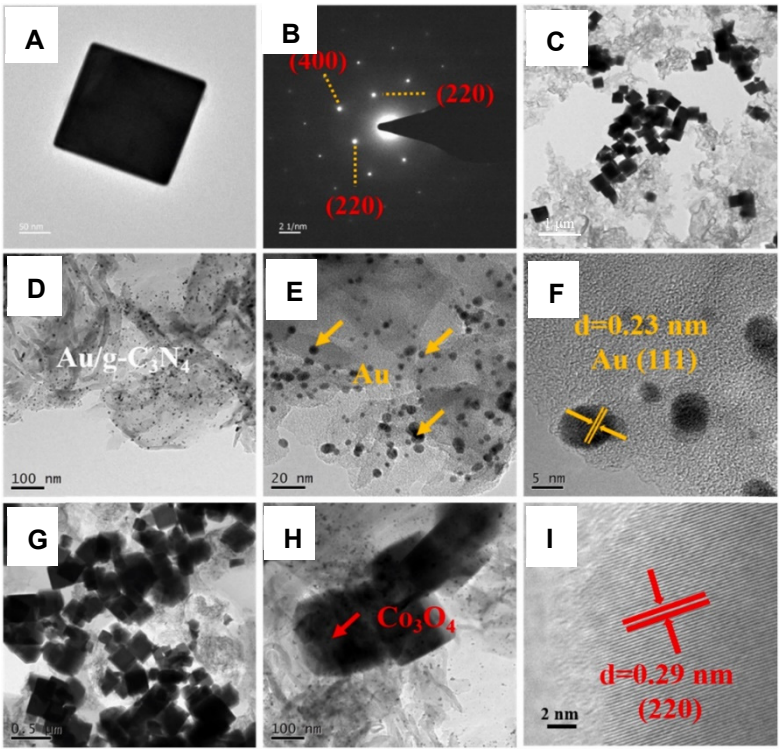

Figure 7. (**A**) TEM photograph and (**B**) SAED pattern of Co_3O_4; TEM photographs of (**C**) CN/Co_3O_4, (**D**–**F**) Au/CN, and (**G**,**H**) $4Au/CN/Co_3O_4$. (**I**) High-resolution TEM photograph of $4Au/CN/Co_3O_4$ [69]. Reprinted with permission from Ref. [69].

Recently, researchers have found that loading single-atom metals as catalysts onto CN can greatly improve the catalytic performance of photocatalysts. Liu et al. dispersed the precursor evenly on the surface of CN by wet chemical means and treated it at low temperature under an inert atmosphere, successfully anchoring Pt atoms in the form of single atoms on the vacancies of carbon nitride. Studies have shown that the introduction of single-atom platinum promotes the separation of photogenerated electrons and holes, reduces recombination, and improves the utilization rate of photoexcited electrons and holes. Single-atom Pt acts as an active center, providing more catalytic sites and accelerating the photocatalytic reaction [70]. Similarly, Zeng et al. prepared interlayer-constrained single Pt atom catalysts by ion exchange. The confinement effect of Pt atoms between CN layers significantly improves the separation efficiency of photogenerated electrons and holes and reduces recombination, thereby enhancing the activity of the photocatalytic reaction to improve its photocatalytic performance [71]. Jin et al. used the cryo-deposition method to disperse $NiCl_2$ in CN material so that Ni atoms can be evenly distributed on CN. By regulating the electronic configuration of Ni single atoms, the photocatalyst exhibits higher photo-response characteristics and conductivity, charge separation efficiency, and mobility under light irradiation. Compared with the unregulated Ni single-atom catalyst, the Ni single-atom catalyst with regulated electronic configuration exhibits higher activity and stability in photocatalytic hydrogen production [72].

In the context of current metal element doping research, due to the high cost of noble metal materials and the relatively weak binding energy between alkali metals, transition metals, and CN, the preparation yield of modified materials is significantly limited, which also hinders the large-scale engineering application. Finally, the comparison table of the most active photocatalysts is listed in Table 3.

Table 3. The element doping of CN for photocatalytic.

Material Type	Synthesis Method	Photocatalytic System	Reference
B-doped CN	Calcination + Hydrothermal	H_2 production	[57]
N-C-O/C-O-C-doped CN	Acid + Hydrothermal	H_2 production	[58]
P, N-doped CN	Hydrothermal	H_2O_2 production	[59]
F-doped CN	Calcination	H_2 production	[60]
B-doped CN	Hydrothermal	H_2 production	[61]
H-doped CN	Hydrothermal	H_2 production	[62]
Fe, Co-doped CN	Hydrothermal	Methylene blue degradation	[63]
Li, Na, K-doped CN	High-temperature assisted	H_2 production	[64]
Fe-doped CN	One-step thermal polymerization	Rhodamine B degradation	[65]
C, P-doped CN	Salt template-induced	H_2 production	[66]
Ag-doped CN	Hydrothermal	H_2 production	[68]
Au-doped CN/Co_2O_3	Hydrothermal	Bisphenol A degradation	[69]
Single atom Pt-CN	Hydrothermal	Sulfonylurea herbicide degradation	[70]
Single atom Pt-CN	Simple cationic ion exchange	H_2 production	[71]
Single atom Ni-CN	Cryo-deposition	H_2 production	[72]

2.4. Heterojunction Construction

Previous studies have shown that the photogenerated electron-hole pairs in a single CN photocatalyst are prone to recombination. By constructing a heterojunction, the recombination of photogenerated electron-hole pairs can be effectively suppressed, mainly by combining heterojunction materials with different energy level structures with CN into a composite photocatalytic material, thereby improving the energy band structure.

The heterojunctions are mainly divided into type I, type II, type Z, and type S, and the widely studied at present are type II and type Z. Type I heterojunction is considered to be an undesirable heterojunction due to its inappropriate band alignment. The type S heterojunction is mainly constructed in a staggered manner using a reduced semiconductor photocatalyst with a smaller work function and a higher Fermi level and an oxidized

semiconductor photocatalyst with a larger work function and a lower Fermi level, which is hard to construct. Yu et al. synthesized an organic conjugated polymer/CN heterojunction to improve the performance of photocatalytic water splitting for hydrogen production. The researchers designed three organic conjugated polymer semiconductor photocatalysts with different electron donor and benzothiadiazole acceptor structural units. By changing the electron donor group in the conjugated skeleton, the band gap of the organic conjugated polymer can be regulated, thereby improving the photocatalytic activity of the organic polymer/CN heterojunction, and the type II heterojunction it forms can promote the separation of electrons and holes, effectively improving the efficiency of photocatalytic hydrogen production [73]. Shi et al. combined highly crystalline CN nanosheets with yolk-shell structured $ZnFe_2O_4$ by solvothermal and calcination methods to form a 2D/3D type II heterojunction. Studies have shown that the conduction band position of CN nanosheets is higher than that of $ZnFe_2O_4$, while the valence band position of $ZnFe_2O_4$ is higher than that of CN. This energy band arrangement enables photogenerated electrons to transfer from the conduction band of CN to the conduction band of $ZnFe_2O_4$, while holes transfer from the valence band of $ZnFe_2O_4$ to the valence band of CN, achieving efficient charge separation and ultimately improving the photocatalytic degradation of tetracycline [74]. Hou et al. prepared the 2D/2D CN/BiOCl (CN/BOC) heterojunction photocatalytic material containing oxygen vacancies by rapid grinding at room temperature using appropriate amounts of CN, bismuth nitrate pentahydrate, glacial acetic acid, and potassium chloride as raw materials. As shown in Figure 8A–H, the experiment shows that the synergistic effect of the heterojunction and oxygen vacancies endows BiOCl/CN with excellent visible light activity. Therefore, BiOCl/CN not only exhibits efficient photocatalytic degradation of organic pollutants but also possesses excellent CO_2 reduction performance [75]. Ahmad et al. prepared a novel type II $MnNb_2O_6$/CN heterojunction photocatalyst using a solvothermal method. The study shows that under light conditions, the formation of the heterojunction promotes the effective separation and transmission of photogenerated electrons and holes. The photogenerated electrons are transferred from the conduction band of CN to the conduction band of $MnNb_2O_6$, while the holes are transferred from the valence band of $MnNb_2O_6$ to the valence band of CN. The separated electrons and holes participate in reduction and oxidation reactions, respectively, generating free radicals with strong oxidizing properties (such as hydroxyl radicals and superoxide radicals), which in turn degrade fluoroquinolone antibiotics [76].

Although type II heterojunction can improve photocatalytic efficiency to a certain extent, it will also lose the strong oxidation or reduction advantages as a single semiconductor. This defect can be overcome by rationally designing the Z-type heterojunction. Chen et al. reported a simple in situ exfoliation and conversion method to uniformly distribute CeO_2 nanoparticles on ultrathin porous CN nanosheets and synthesize a novel Z-type CeO_2/CN heterojunction. Studies have shown that the ultrathin porous structure of CN can not only increase the specific surface area to provide more active sites but also effectively shorten the migration distance of photogenerated electrons and holes to avoid recombination. At the same time, the highly dispersed CeO_2 and CN have close interface contact, which enables more charges to be transferred through the interface. In addition, the synthesized CeO_2/CN heterostructure has a bandgap-matched Z-type structure, which can effectively prolong the lifetime of photoinduced charge carriers and enhance the redox ability of the photocatalyst, ultimately achieving an improvement in the photocatalytic reduction of CO_2 [77]. Meng et al. used a simple room temperature stirring deposition method to controllably prepare a dual-channel Z-type ZIF-L/CN heterojunction, achieving effective separation of photogenerated holes and electrons, and at the same time constructed a piezoelectric-photocatalytic reaction system based on the ZIF-L/CN heterojunction. Research has shown that with the assistance of ultrasonic energy, a polarized electric field is formed between the catalyst bulk and the interface, which provides a strong driving force for the directional migration of carriers at the heterojunction interface, thus achieving efficient H_2O_2 catalytic synthesis in a pure water system. In addition, experimental characterization and DFT calculations have

demonstrated that the synergistic effect between the Z-type heterostructure and the electric field can significantly improve the H_2O_2 catalytic activity of the material [78]. Sun et al. first prepared the original CN by molecular self-assembly method. Subsequently, the acid-treated CN and $BiVO_4$ nanosheets were combined in a hydroxyl-induced manner to form a $BiVO_4$/CN (BVO/CN) Z-type heterojunction, and the CoOx nanoclusters were controllably modified on CN. Finally, a CoOx-BVO/CN heterojunction photocatalytic material with efficient charge separation and synergistic catalytic ability was realized, which showed excellent performance in the reduction of CO_2 [79]. Chen et al. loaded Ag_3PO_4 on the surface of CN by a simple in-situ deposition method to form a CN/Ag_3PO_4 heterojunction. Studies have shown that under visible light irradiation, CN and Ag_3PO_4 are excited to generate photogenerated electrons and holes, respectively. Due to the existence of the Z-type heterojunction, the photogenerated electrons in the conduction band of CN can be quickly transferred to the valence band of Ag_3PO_4 to recombine with holes, thereby inhibiting the recombination of photogenerated electrons and holes. The holes in the valence band of CN and the electrons in the conduction band of Ag_3PO_4 participate in oxidation and reduction reactions, respectively, generating free radicals with strong oxidizing properties, ultimately achieving efficient photocatalytic degradation of ofloxacin [80]. Similarly, Du et al. assembled CN and $W_{18}O_{49}$ into a nanocone array structure through a special preparation process. This structure not only increases the specific surface area of the catalyst but also promotes multiple reflections and light scattering inside the catalyst, thereby improving the absorption and utilization efficiency of light. Research shows that the catalyst exhibits strong absorption capabilities in the ultraviolet-visible-near-infrared (UV-Vis-NIR) spectrum range. In particular, the introduction of $W_{18}O_{49}$ significantly enhances the absorption of infrared light. In addition, the introduction of $W_{18}O_{49}$ not only serves as an infrared light absorption material but also promotes the separation and migration of photogenerated charges through the LSPR effect. At the same time, the Z-type heterojunction formed by $W_{18}O_{49}$ and CN further improves the charge separation efficiency [81]. Eroglu et al. constructed a complex type II heterojunction with CN, black phosphorus (BP), and graphene quantum dots (GQDs), and a GQDs@CNBP heterojunction with the kinetic rate constants of 0.1415 min^{-1} (30 min) for methyl orange (MO) and 0.0371 min^{-1} (120 min) for TC is one of the highest kinetics that has been reported in the literature so far [82]. Alemdar et al. fabricated binary red phosphorus/CN (RP/CN) heterojunctions decorated with Pt nanoparticles (denoted Pt/RP/CN) with a facile ultrasound-assisted two-step protocol as a photo-assisted catalyst for the hydrolysis of ammonia borane (HAB) and reach a superb H_2 generation rate of 142 mol H_2·mol Pt^{-1}·min^{-1} under visible light irradiation [83]. Finally, the comparison table of the most active photocatalysts is listed in Table 4.

Table 4. The heterojunction construction of CN for photocatalytic.

Material Type	Synthesis Method	Photocatalytic System	Reference
Fluorene, carbazole, *N*-annulated perylene-CN	Calcination + Hydrothermal	H_2 production	[73]
$ZnFe_2O_4$/CN	Solvothermal + Calcination	Tetracycline degradation	[74]
BiOCl/CN	Grinding	H_2 production	[75]
$MnNb_2O_6$/CN	Solvothermal	Fluoroquinolone degradation	[76]
CeO_2/CN	In situ exfoliation	CO_2 reduction	[77]
ZIF-L/CN	Stirring deposition	H_2O_2 production	[78]
CoOx-BVO_4/CN	Molecular self-assembly	CO_2 reduction	[79]
Ag_3PO_4/CN	In-situ deposition	Ofloxacin degradation	[80]
$W_{18}O_{49}$/CN	Hydrothermal	H_2 production	[81]
GQDs@CNBP	Ultrasonic + Exfoliation	MO degradation	[82]
Pt/RP/CN	Ultrasound-assisted two-step protocol	H_2 production	[83]

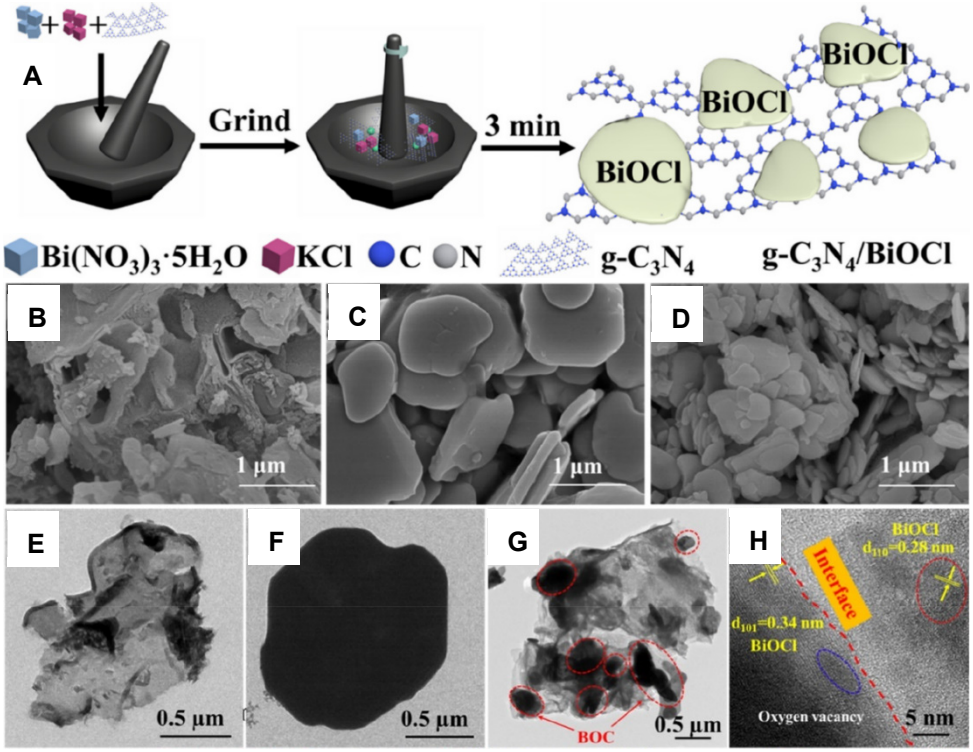

Figure 8. (**A**) Synthesis processes of 2D/2D CN/BiOCl heterostructure materials; SEM images of (**B**) CN, (**C**) BOC, and (**D**) CN/BOC-5; TEM images of (**E**) CN, (**F**) BOC, and (**G**) CN/BOC-5; (**H**) HRTEM image of CN/BOC-5 [75]. Reprinted with permission from Ref. [75].

3. The Research Progress on Photocatalytic Applications of CN

3.1. Photocatalytic Degradation of Organic Pollutants

The harmful substances contained in wastewater discharged by industrial production are gradually polluting the natural environment on which human beings depend for survival and will cause lasting harm to the human body. Currently, the toxic pollutants contained in water bodies mainly include heavy metals and organic pollutants. In recent years, photocatalytic technology has been widely used to reduce heavy metals and degrade organic pollutants. Yin et al. constructed a 3D $MgIn_2S_4$ nanoflower/2D oxygen-doped CN nanosheet heterojunction catalyst. This direct Z-type heterostructure design combines the advantages of both materials. The 3D $MgIn_2S_4$ nanoflower structure provides a large specific surface area, which is conducive to the adsorption and reaction of reactant molecules, while the 2D oxygen-doped CN nanosheets enhance light absorption and charge transfer capabilities due to their unique electronic structure and optical properties. The results show that all hybrid photocatalysts exhibit superior Cr (VI) photoreduction performance when compared with single components. The efficiency of photocatalytic reduction of Cr (VI) of the best junction sample reached 99.1%, which was 2.0 and 343.7 times higher than that of 3D $MgIn_2S_4$ nanoflowers and 2D oxygen-doped CN nanosheets, respectively. This indicates that the synergistic effect of the composite material significantly improved the photocatalytic efficiency [84]. Xu et al. synthesized lignin-derived C-doped CN (LCN) by direct calcination of lignin and melamine physically blended. The photocatalytic effect of tetracycline hydrochloride (TC) and peroxymonosulfate (PMS)-assisted photocatalytic effect on typical organic pollutants under visible light was studied. Studies have shown that TC will not self-degrade under light and the photocatalytic efficiency of CN is significantly improved with the introduction of C. In the system where photocatalysis and PMS coexist, the catalyst has a significant degradation effect on TC. Compared with undoped CN (MCN), LCN exhibits strong light absorption and efficient charge transfer. PMS captures electrons to promote the transfer of electron-hole pairs, thereby generating reac-

tive oxygen species (ROSs) and improving the photocatalytic efficiency [85]. Zeng et al. fabricated nitrogen vacancies and oxygen substitution-modified CN ((Nv, Os)-CN) with a rearranged surface via a low-temperature thermal oxidation strategy. Under visible light irradiation, (Nv, Os)-CN can effectively degrade TC, ciprofloxacin (CIP) and sulfadiazine (SZO) than CN. The first-order kinetic constants of (Nv, Os)-CN for TC, CIP, and SZO are 2.1, 2.24, and 1.38 times higher than those of CN, respectively. This high performance is attributed to the rearranged surface atoms, which form an active surface rich in Nv and Os, thereby promoting interfacial charge transfer and establishing a strong water-(Nv, Os)-CN interface [86]. Zhang et al. prepared a novel 5-bromo-2-thiophenecarboxaldehyde (BTC) grafted carbon nitride photocatalyst (TCN). The results show that this material has obvious performance advantages. Compared with ordinary CN, the photocatalytic rate constant of oxytetracycline degradation by TCN-5 increased by about 2.32 times, and the degradation efficiency is as high as 93%. At the end of the reaction (60 min), the TOC mineralization rate reaches 38% [87]. Kuate et al. successfully prepared a 2D/3D black CN (CN-B)/BiOI S-type heterojunction photocatalyst using a simple hydrothermal method. As shown in Figure 9A–F, the prepared composite photocatalyst is approximately spherical with burrs on the surface, and the particle size exceeds 1 μm. The catalyst has good photocatalytic activity for the degradation of TC antibiotics in irradiated simulated seawater. As shown in Figure 9G–J, by adjusting the ratio of CN-B, the optimal 10% CN-B/BiOI achieves a TC degradation efficiency of about 93% within 60 min, which is significantly higher than that of pure CN-B and BiOI. Its degradation rate constant is 0.0389, which is much higher than 0.0142, 0.0222, and 0.0291 of ordinary CN, CN-B, and BiOI, respectively. Finally, the stability test showed that after four cycles of degradation tests, the degradation activity of 10% CN-B/BiOI remained basically unchanged, demonstrating the excellent photocatalytic performance of CN-B/BiOI [88].

In addition to degrading organic pollutants antibiotics, the excellent CN photocatalytic material can also effectively degrade organic dyes. Ganesan et al. modified CN by direct thermal exfoliation (TE-CN) and studied the photocatalytic degradation efficiency towards textile dyes such as methylene blue (MB), MO, and rhodamine B (RhB). The specific surface area analysis of CN and TE-CN shows that the specific surface area of the TE-CN sample (48.20 m^2/g) is higher than that of bulk CN (5.03 m^2/g) and the adsorption efficiency of TE-CN is 2.98 times that of bulk CN. In addition, the study indicates that TE-CN has excellent stability over five degradation cycles, with its activity only decreasing from 92% to 86.2% [89]. Huang et al. used different acids to treat dicyandiamide and prepared thin-layer porous CN rich in amino groups by precursor modification and applied it to the degradation of RhB. Experiments have shown that CN prepared by modifying dicyandiamide with concentrated nitric acid (5H-CN) exhibits the best degradation effect, and its degradation rate of RhB is 34 times higher than that of unmodified bulk CN [90]. Song et al. discovered through experiments and calculations that porous CN nanosheets have a larger specific surface area and abundant active sites, which can effectively improve the efficiency of charge transfer and separation and also optimize the photoredox energy. Based on this, the research team synthesized a special organic dye-modified melamine precursor and then prepared porous defect-modified CN nanosheets to improve the photocatalytic activity. Experiments show that the CN product prepared by modifying melamine precursor with seven organic dyes (such as 4-nitrophenol, RhB, R6G, MO, MB, crystal violet, and malachite green) can simultaneously integrate the advantages of porous structure and defects, thereby achieving higher photocatalytic degradation efficiency for RhB dye. When it comes to CN prepared from 4-nitrophenol-modified melamine precursor, its optimal photocatalytic degradation reaction rate constant is 0.5324, which is 29.6 times that of ordinary bulk CN [91]. Li et al. constructed an S-type heterojunction of N-doped carbon dots (NCDs) and S-doped CN (S-CN) through π-π conjugated self-assembly, in which the S-doped CN has a larger specific surface area and can enhance the absorption of visible light by adjusting the band gap, while the N-doped carbon quantum dots (CQDs) can effectively promote charge separation and transfer. As shown in Figure 10A–D, experimental calculations show that

NCDs/S-CN-1.00 can degrade RhB by 99% within 15 min, which is much greater than the 71% of S-CN. Within 180 min, p-nitrophenol (PNP) can be degraded by 92%, which is much greater than the 63% of S-CN, and the degradation kinetic constants for RhB and PNP are 2.72 and 2.65 times than that of S-CN, respectively. As shown in Figure 10E, the mechanism study shows that the improvement of photocatalytic performance is mainly due to the formation of an S-type heterojunction between S-CN and NCDs. The formed internal electric field, the interaction of π-π conjugated bonds, and the effect of band bending promote the recombination of photogenerated electrons and holes with low redox ability but retain the beneficial electrons and holes with strong redox ability, which helps to produce more active species h^+ and $\cdot O_2^-$, thereby significantly improving the ability of photocatalytic degradation of organic matter [92]. Xiong et al. obtained reduced graphene oxide-modified black phosphorus quantum dots (rGO@BPQDs) through surface modification of BPQDs with rGO via an ultrasound-assisted liquid phase method and remarkably improved the photoelectric properties of CN. Likewise, the kinetic constant of RhB and tetracycline degradation reached 0.183 and 0.0194 min^{-1}, respectively [93]. Finally, the comparison table of the most active photocatalysts is listed in Table 5.

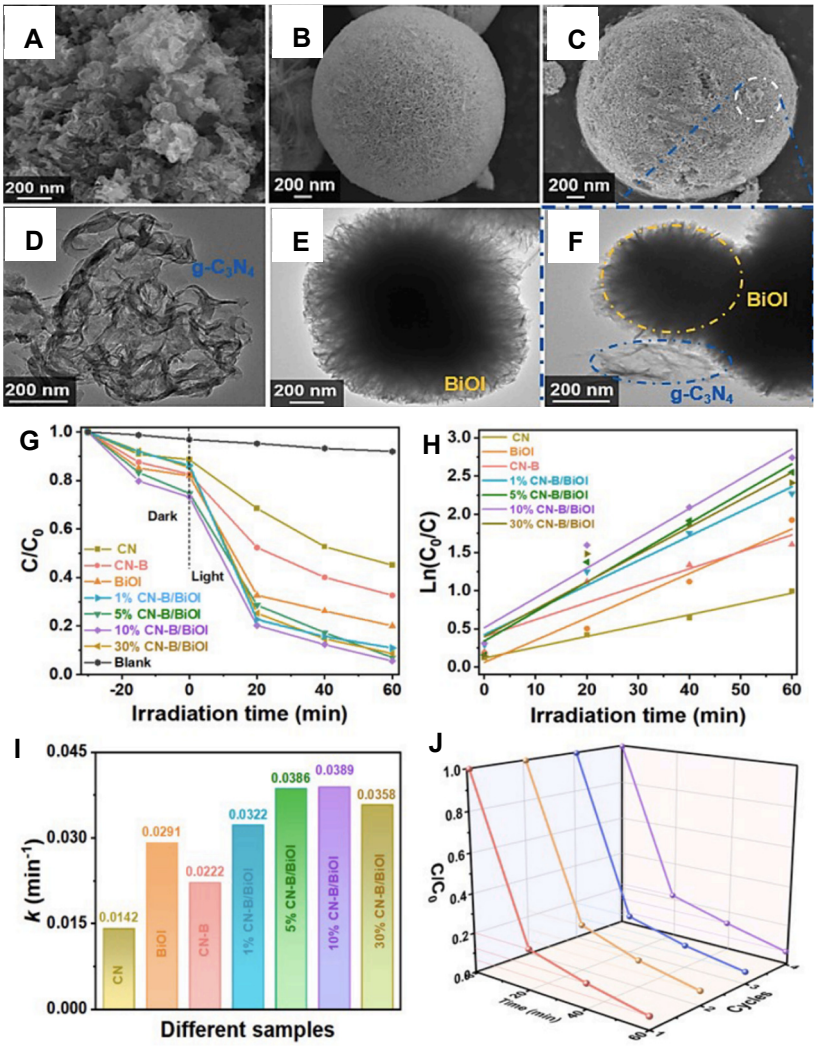

Figure 9. SEM images of (**A**) CN-B, (**B**) BiOI, and (**C**) 10% CN-B/BiOI composite; TEM images of (**D**) CN-B, (**E**) BiOI, and (**F**) 10% CN-B/BiOI composite; (**G**) Photocatalytic TC degradation curves of the as-prepared photocatalysts in simulated seawater. (**H**) Pseudo-first-order degradation kinetics curves and (**I**) corresponding degradation rate constants of the prepared samples. (**J**) Photocatalytic TC degradation stability tests of 10% CN-B/BiOI sample [88]. Reprinted with permission from Ref. [88].

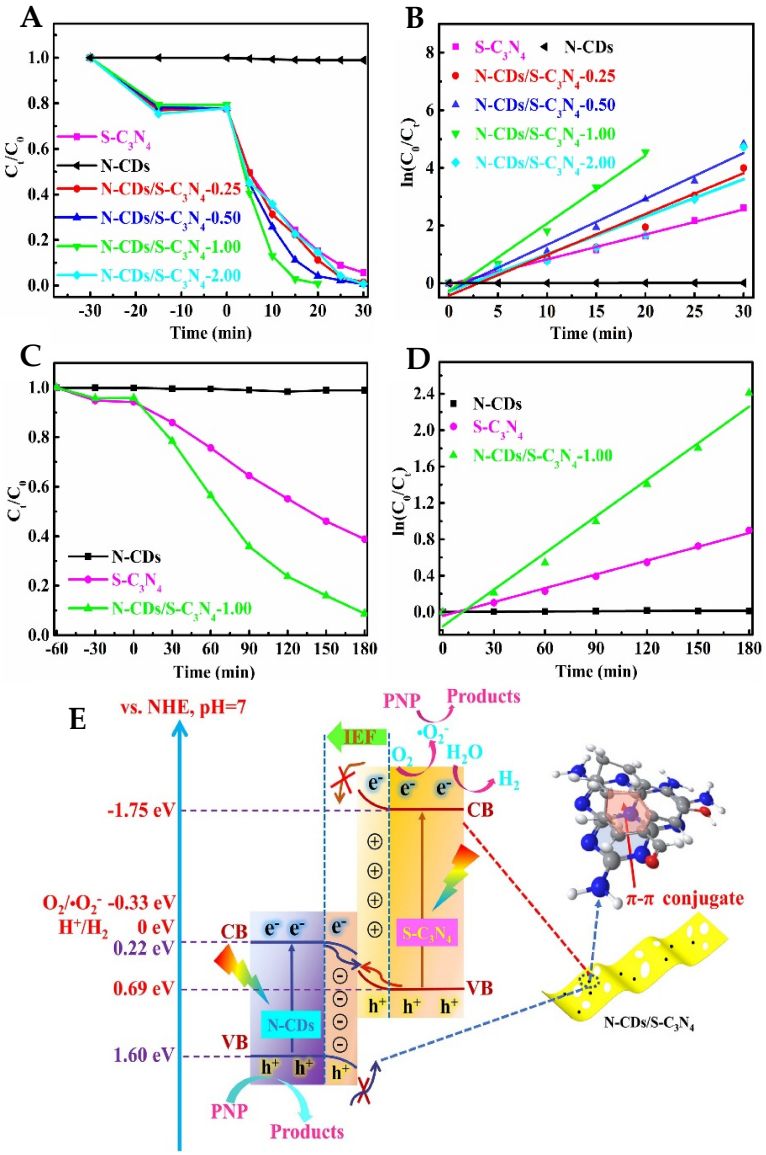

Figure 10. Photodegradation of RhB under visible-light irradiation (**A**) and corresponding first-order plots (**B**); Photodegradation of PNP under visible-light irradiation (**C**) and corresponding first-order plots (**D**); (**E**) Photocatalytic mechanism of N-CDs/S-CN S-scheme heterojunction [92]. Reprinted with permission from Ref. [92].

Table 5. The photocatalytic activities for organic degradation of CN.

Material Type	Degradation System	Photocatalytic Performance	Reference
$MgIn_2S_4$ nanoflower/2D oxygen-doped CN	Cr (VI) solution	343.7-fold enhancement	[84]
C-doped CN	TC solution	6.74-fold enhancement	[85]
Nv, Os-CN	TC, CIP, SZO solution	2.1, 2.24, 1.38-fold enhancement	[86]
BTC/CN	Oxytetracycline solution	2.32-fold enhancement	[87]
BiOI/CN-B	TC solution	93% removal rate in 60 min	[88]
TE-CN	MB, MO, RhB dyes	92%, 93%, 95% removal rate in 60 min	[89]
5H-CN	RhB dyes	34-fold enhancement	[90]
4-nitrophenol-modified CN	RhB dyes	29.6-fold enhancement	[91]
NCDs/S-CN	RhB dyes	99% removal rate in 15 min	[92]
rGO@BPQDs/CN	RhB/tetracycline solution	2.69-fold enhancement	[93]

3.2. Photocatalytic Hydrogen Production

In the field of new energy, hydrogen energy is generally considered to be a clean green energy, and its reserves in nature are very abundant. In general, when a semiconductor is irradiated by ultraviolet light or visible light, and the input light energy is greater than the bandgap width of the semiconductor, electrons will be excited from the valence band to the conduction band to generate electron-hole pairs. The electrons and holes react with water molecules to generate H_2 and O_2, thereby achieving photocatalytic hydrogen production. In 2009, Wang et al. proposed the use of CN for photocatalytic hydrogen production and achieved certain results [13]. Since then, researchers have extensively carried out research on photocatalytic hydrogen production by continuously modifying CN. Zhang et al. designed and synthesized Pt@Au nanorods (Au NRs)/CN photocatalyst using the LSPR effect of the precious metal Au. The results show that the LSPR effect of Au and the synergistic effect of Pt-Au together enhanced the hydrogen production rate of CN [94]. Similarly, Yan et al. deposited Ag nanoparticles and Ni nanoparticles on single CN nanoparticles using a two-step synthesis method and were independently dispersed on CN. The results of photocatalytic reduction hydrogen production show that the photocatalytic activity of bimetallic loaded CN is nearly 12 times higher than that of Ni/CN sample with the same loading mass, and nearly 4 times higher than that of Ag/CN sample with the same loading mass. Further mechanism studies show that during the preparation process of loading Ag by photoreduction, holes are transported to Ni nanoparticles and reacted on them, while CN gathers electrons to reduce Ag ions and load them on it. Two heterojunctions, Ni/CN and Ag/CN, are formed on a single CN nanoparticle. These two heterojunctions produce a synergistic effect and form a long-range electric field on the CN nanoparticle, thereby greatly improving the carrier separation rate [95]. Yang et al. prepared CN intermolecular homojunction (UTMCN) by alkali metal salt (NaCl + KCl)-assisted multi-precursor (urea + thiourea + melamine) co-thermal polymerization technology, forming a unique triple S-scheme type energy band arrangement to promote the efficient separation of photogenerated carriers. As shown in Figure 11A–C, the photocatalytic hydrogen production results show that UTMCN has excellent photocatalytic performance, exhibiting a hydrogen production rate of 5281 $\mu mol^{-1}g^{-1}h^{-1}$, which is about 38.9 times that of bulk CN. To demonstrate the reusability of the synthesized samples, four consecutive cyclic stability tests were conducted, and the UTMCN still maintains a high catalytic activity even after 12 h of continuous testing. In addition, the authors also combined DFT to study the intrinsic mechanism of enhanced photocatalytic hydrogen production performance. As shown in Figure 11D–I, when an intermolecular homojunction is formed, the electrons in the T region and the M region are transferred to the U region, thereby forming a space charge layer at the interface. In the process of the Fermi level re-balancing, the flow of electrons forms a strong built-in electric field at the contact interface, causing the photogenerated charges to be transferred along an S-shaped route, which is conducive to the dissociation of excitons and the separation and transfer of photogenerated electrons and holes. In addition, it has been calculated that the built-in electric field strength of UTMCN is 12.18 times that of bulk CN [96]. Wang et al. reported a self-assembly method to synthesize S-doped CN through the self-assembly of melamine and thiocyanate and then calcined it to obtain S-doped CN. Although the S-doped CN obtained by this method contains only a small amount of sulfur dopant (0.14 wt.%), it has high crystallinity (even higher than that of the original CN) and a broadened visible light response range. During and after calcination, the high melting point melamine-trithiocyanate supramolecular precursor effectively maintains the ordered structure of the crystal, resulting in a product with high crystallinity. Experiments show that the optimal S-doped CN (MTCN-6) exhibits an ultrahigh H_2 production rate of 1511.2 $\mu mol^{-1}g^{-1}h^{-1}$ under visible light excitation, which is approximately 11 times that of the original CN [97]. He et al. first synthesized 3D C using in-situ chemical vapor deposition, then mixed urea with 3D C aqueous solution, and finally calcined it to obtain the 3D C/CN composite material. Studies have shown that this unique structure can prevent

the aggregation and stacking of CN nanosheets, while also providing a multi-directional transmission path for electrons, thereby improving light absorption by increasing the number of light reflections. In addition, the close contact interface between CN and 3D C facilitates the transfer of photogenerated electrons from CN to 3D C. Therefore, due to the combined effects of reduced nanosheet thickness, abundant active sites, enhanced visible light utilization, and increased interface contact area, the photocatalytic performance of 3D C/CN materials for hydrogen production has been improved. The optimal 3D C/CN photocatalytic material shows a hydrogen evolution rate as high as 1610 $\mu mol^{-1}g^{-1}h^{-1}$, which is nearly 7 times that of bulk CN (240 $\mu mol^{-1}g^{-1}h^{-1}$) [98]. In order to solve the serious carrier recombination problem caused by electron-hole Coulomb interaction in CN polymers, Yang et al. synthesized ultra-small CN photocatalysts (SS-CNPs) and constructed a CN photocatalyst system with small-sized CN aggregates through non-covalent self-assembly, achieving a record apparent quantum efficiency and excellent photocatalytic activity. The characterization results indicate that SS-CNPs obtain persistent charges through non-covalent interactions, thus breaking the symmetry. SS-CNP spontaneously breaks the symmetry to achieve asymmetrically distributed charges, thus generating a built-in electric field inside the material, thereby accelerating charge separation and improving carrier lifetime. The photocatalytic results show that the apparent quantum efficiency of the SS-CNPs aggregate photocatalyst reached a record as high as 76.4% at 420 nm, which is better than that of the existing CNP photocatalyst system [99]. Wu et al. used a coordinated regulation strategy to prepare a 3D honeycomb CN (Cr-PHCN) photocatalyst material with seamless splicing of carbon rings (Cr) in the plane through a simple chemical vapor deposition method in an air atmosphere by one-step co-condensation. The test results show that the specific surface area of Cr-PHCN is 68.12 $m^2 \cdot g^{-1}$, which is much higher than the 8.09 $m^2 \cdot g^{-1}$ of ordinary CN. The large specific surface area and pore volume are beneficial to provide more catalytic active reaction sites, while the thin wall is conducive to the rapid transport of electrons. Moreover, multiple refraction and scattering of incident light inside the honeycomb can effectively enhance light utilization. From the perspective of electronic structure regulation, the extended π-conjugated system of triazine/Cr in the Cr-PHCN crystal structure can promote $n \rightarrow \pi^*$ electron migration, which has a positive effect on accelerating carrier transport and promoting electron-hole pair separation. Therefore, under the coordinated regulation of 3D morphology construction and in-plane electronic modification, photocatalytic performance has achieved a breakthrough. The average hydrogen production rate of Cr-PHCN reaches a maximum of 7581 $\mu mol^{-1}g^{-1}h^{-1}$, which is much higher than the 160 $\mu mol^{-1}g^{-1}h^{-1}$ of ordinary CN [100]. Finally, the comparison table of the most active photocatalysts is listed in Table 6.

Table 6. The photocatalytic activities for H_2 production of CN.

Material Type	Sacrificial Agent	Photocatalytic Performance	Reference
Pt@Au NRs/CN	10 mL deionized water	207.0 $\mu mol\ h^{-1}$ (20 mg)	[94]
Ag/Ni/CN	10 mL methanol	600 $\mu mol^{-1}g^{-1}h^{-1}$	[95]
UTMCN	10 vol% triethanolamine	5281 $\mu mol^{-1}g^{-1}h^{-1}$	[96]
S-doped CN	10 mL deionized water	1511.2 $\mu mol^{-1}g^{-1}h^{-1}$	[97]
3D C/CN	10 mL triethanolamine	1610 $\mu mol^{-1}g^{-1}h^{-1}$	[98]
SS-CNP/BA	10 vol% triethanolamine	272.4 $\mu mol\ h^{-1}$ (2 mg)	[99]
Cr-PHCN	45 mL triethanolamine	7581 $\mu mol^{-1}g^{-1}h^{-1}$	[100]

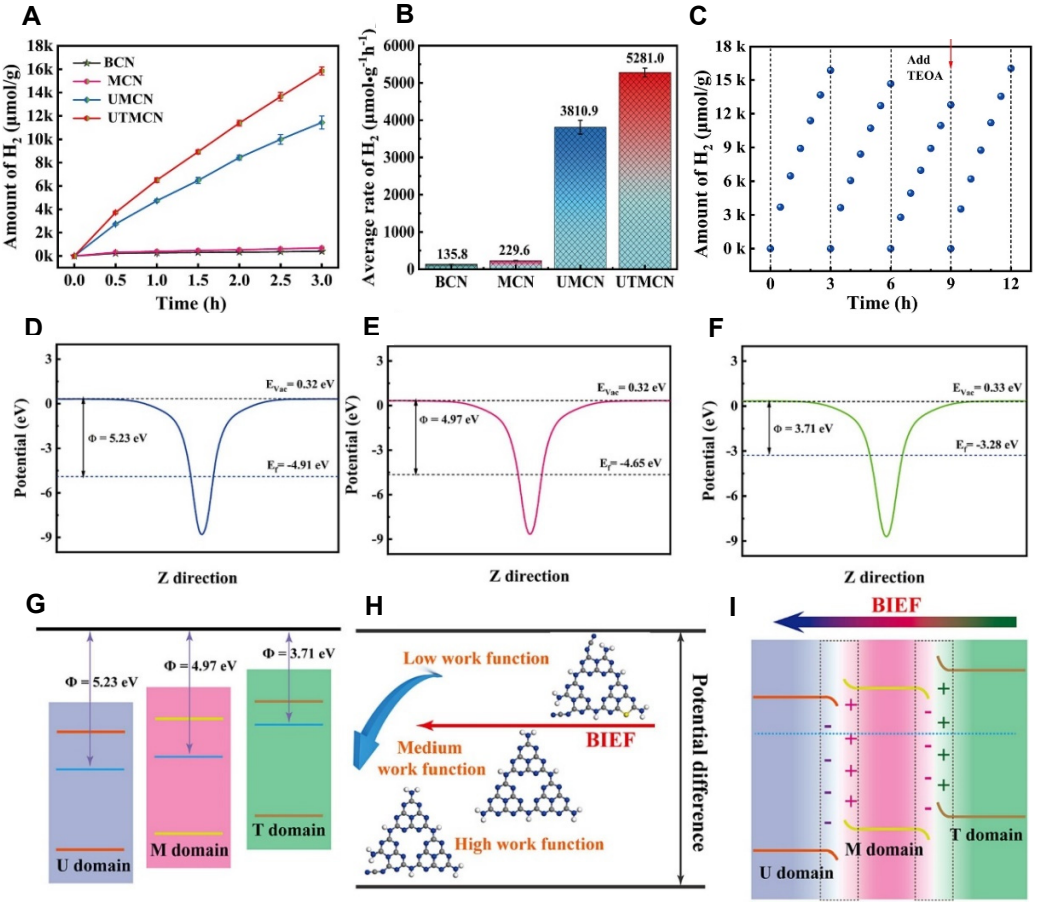

Figure 11. (**A**) The photocatalytic hydrogen production over 3 h and (**B**) the corresponding hydrogen evolution rate of BCN, MCN, UMCN and UTMCN; (**C**) Stability evaluation of photocatalytic hydrogen production for UTMCN; The theory work function of (**D**) U domain, (**E**) M domain and (**F**) T domain; (**G**–**I**) The built-in electric field (BIEF) formation by U domain, M domain and T domain [96]. Reprinted with permission from Ref. [96].

3.3. Photocatalytic Reduction of CO_2

CO_2 is one of the most important factors leading to global warming. How to reasonably solve the environmental problems caused by CO_2 gas will affect the sustainable development of society and the economy. Normally, CO_2 molecules are very stable, it takes about 750 kJ·mol^{-1} of dissociation energy to break the C=O bond. It is very difficult to treat CO_2 using conventional physical and chemical methods. However, there are isolated electron pairs around O in the CO_2 molecule, which can provide electrons to the Lewis acid center, while C can accept electrons from the Lewis base [7,8]. In addition, CO_2 can also be adsorbed on the surface of most catalysts. Under the stimulation of sunlight, the catalyst material can induce CO_2 to convert into high-value hydrocarbon fuels, which can not only alleviate the greenhouse effect but also produce high-value-added industrial products.

In recent years, researchers have modified CN to make it have a stronger ability of photocatalytic reduction of CO_2. In order to solve the problem of insufficient CO_2 adsorption activation sites in bulk CN, Li et al. used a simple one-step hydrothermal method to achieve CQDs and oxygen atom doping co-modification of CN. Mechanism studies have shown that CQD modification not only facilitates charge transfer and separation but also provides a large number of CO_2 adsorption and activation sites. In addition, the process of oxygen atom doping in CN (OCN) leads to the formation of nitrogen defects, which can promote the dissociation of water and the oxidation half-reaction, and sustainably provide H^+. The photocatalytic results show that CQDs/OCN-x (x represents the volume ratio of H_2O_2 (30 wt.%) in the mixed solution used in the laboratory) achieve excellent

CH_4 selectivity in the photocatalytic reduction of CO_2, with a cumulative CH_4 production of 1.2 $\mu mol^{-1}g^{-1}h^{-1}$ within 8 h, which is nearly 14 times higher than that of ordinary CN [101]. Hu et al. successfully anchored different numbers of Ag single atoms on hollow porous polygonal CN nanotubes (PCN) through a simple "impregnation+pyrolysis" process to form Ag1@PCN photocatalysts with Ag N3 coordination for CO_2 photoreduction with H_2O as the reductant. The morphology characterization results show that Ag1@PCN has a polygonal tubular structure with a length of about 12 μm and a width of about 2 μm, and there are a large number of pores in the hollow polygonal tubular structure, which is conducive to the adsorption of CO_2. The results of photocatalytic production of CH_4 and CO show that the introduction of a single Ag atom significantly improves the performance of Ag1(x)@PCN (x: mass percentage of Ag, wt%). With the increase in Ag1(x)@PCN, the evolution rates of CH_4 and CO increased, and the Ag1(0.73)@PCN is the best, reaching 0.021 and 0.320 $\mu mol^{-1}g^{-1}h^{-1}$, respectively, the latter is nearly 12 times that of ordinary PCN. Combined with the DFT calculation results, it can be shown that the strong metal support interaction in the AgN3 configuration can promote the transfer dynamics of photoexcited carriers. In addition, single Ag atoms can also serve as active sites to enhance CO_2 adsorption and reduce the barrier from $*CO_2$ to *COOH, thereby enhancing CO_2 photoreduction activity and CO selectivity [102]. Double-atom-dot catalysts (DACs) have higher metal content and more active sites than single-atom-dot catalysts. Ma et al. first constructed Rh_2 DAC (Rh_2/HCNS-Nv) on loose and porous CN hollow nanospheres containing N vacancies and applied it to the photocatalytic CO_2 reduction reaction, overcoming the current limitation of low electron-hole recombination rate and prolonging the lifetime of photogenerated carriers. Studies have shown that the high specific surface area of hollow nanospheres is conducive to the uniform dispersion and anchoring of Rh_2 diatomic pairs, and the N vacancies induce the formation of a stable 3N/Rh-Rh/1N2C coordination between the carrier and the Rh_2 diatomic pairs. The localized charge on the carrier with N vacancies is transferred to the Rh_2 diatomic site through the 3N/Rh-Rh/1N2C bridge, making the charge-rich Rh_2 diatomic site the active center of the reaction, thus improving the charge separation efficiency of Rh_2/HCNS-Nv. Due to the synergistic effect of support modification and Rh_2 diatomic sites, Rh_2/HCNS-Nv exhibited high CO/CH_4 release activity and high CH_4 selectivity in the photocatalytic reduction in CO_2. Further DFT calculations confirm that, compared with Rh_1 SAC, Rh_2 DAC can effectively stabilize the rate-limiting intermediate CHO* and well weaken the CO bond strength in the CH_3O* intermediate, thus promoting the generation and separation of CH_4, the maximum yields of CH_4 and CO are 14.16 and 5.16 $\mu mol^{-1}g^{-1}h^{-1}$, respectively, with a CH_4 electron selectivity of 91.65% [103]. Wan et al. constructed a novel CN/La, Rh co-doped $SrTiO_3$ (CN/LRSTO) S-type heterojunction for photocatalytic CO_2 reduction using an electrostatic self-assembly method. With the help of the built-in electric field at the S-type heterojunction interface, the recombination of photogenerated electrons and holes is significantly suppressed, and the redox ability of photogenerated carriers is significantly improved, thereby efficiently catalyzing the reduction in CO_2 to CO and CH_4. For the optimized S-type heterojunction CN/LRSTO-30wt%, the average production rates of the products CO and CH_4 are 4.1 $\mu mol^{-1}g^{-1}h^{-1}$ and 1.8 $\mu mol^{-1}g^{-1}h^{-1}$, respectively, which are about 1.9 times and 22.5 times higher than those of pure CN, respectively. In addition, the S-type heterojunction still has high catalytic activity after three cycle tests, indicating its good stability. Subsequently, the authors used in situ XPS to further study the photogenerated electron-hole separation and transfer mechanism in the CN/LRSTO-30wt% S-type heterojunction. Since the surface work function of LRSTO is smaller than that of CN, after they come into contact, it is easier for electrons in LRSTO to escape from its surface and transfer to CN, thus forming a built-in electric field pointing from LRSTO to CN, and the corresponding energy band bends at the contact interface. When illuminated, since both CN and LRSTO have light absorption, the photogenerated electrons of CN will rapidly recombine with the photogenerated holes of LRSTO under the promotion of the built-in electric field. Under the hindrance of the built-in electric field, the recombination between

the photogenerated electrons of LRSTO and the photogenerated holes of CN is greatly suppressed. Therefore, the lifetime of the photogenerated carriers in the heterojunction is greatly prolonged, and the reduction and oxidation abilities of the corresponding photogenerated electrons and holes are enhanced, which will greatly promote the photocatalytic CO_2 reduction process [104].

Hussien et al. used a green and simple method to synthesize a new type of ultrathin porous material of phosphorus and boron-doped CN, which has strong photocatalytic CO_2 reduction activity, especially for selective CO generation. The study shows that the optimized electronic structure and porous morphology due to the presence of dual non-metallic dopants extend the optical path, thereby improving the visible light harvesting capability. At the same time, the coexistence of electron-deficient atoms (B) and electron-rich Lewis acid centers (P), as well as the presence of Lewis basic functional groups (NH_2) as photoinduced charge carrier separation centers, promotes charge separation. In addition, with the help of fast charge transfer and injection of ultrathin nanosheets, the charge migration distance and a large number of point and body defects are reduced. Finally, under visible light irradiation, the CO yield can be increased to 22.45 $\mu mol^{-1}g^{-1}h^{-1}$, which is about 12 times that of the original CN [105]. Yang et al. constructed a compact 2D/2D CN@BiOI S-type heterojunction on hydrophobic carbon fiber paper for efficient CO_2 photoreduction. Studies have shown that the design of the S-type heterojunction promotes the separation of photogenerated electrons and holes and reduces their recombination rate. Further, the formation of a gas-liquid-solid three-phase interface facilitates the effective adsorption and reaction of CO_2 and water molecules on the catalyst surface, thereby improving the rate and efficiency of the photocatalytic reaction. The prepared heterojunction has good CO selectivity (77.8%) and activity (458.0 $\mu mol\ h^{-1}m^{-2}$), which is significantly better than the traditional photocatalytic system, indicating that the design of the S-type heterojunction and the gas-liquid-solid three-phase interface plays an important role in improving the photocatalytic performance [106]. Ding et al. constructed a heterojunction system consisting of CN-encapsulated melamine-resorcinol-formaldehyde (MRF) microspheres using a simple one-pot hydrothermal method, labeled as XCN@M, where X is the weight (%) of CN, and evaluated their activity for photocatalytic reduction in CO_2. The photocatalytic results show that the yield of CH_3OH is 0.99 $\mu mol\ h^{-1}$ when using 100 mg photocatalyst containing 15wt% CN at a reaction temperature of 80 °C and 0.5 MPa, and the external quantum efficiency is 5.5% at 380 nm and 1.7% at 550 nm, which is about 20 times and 10 times higher than that of CN and MRF, respectively. XPS, TEM, and EDS analysis were further utilized to demonstrate the formation of the core-shell structure and the charge transfer on the CN bond at the CN-MRF interface as well as the charge transfer between the methoxy group of the 2,4-dihydroxymethyl-1,3-diphenol part in MRF and the terminal amino group in CN. This enhanced ligand-ligand charge transfer results in 67% of the photoexcited internal charges in the MRF being transferred from the CN to the hydroxymethylamino groups, which are the catalytic sites for the photocatalytic reduction in CO_2 to CH_3OH, thus effectively improving the activity of the photocatalytic reduction in CO_2 [107]. Finally, the comparison table of the most active photocatalysts is listed in Table 7.

Table 7. The photocatalytic activities for CO_2 reduction in CN.

Material Type	Reduction Product	Photocatalytic Performance	Reference
CQDs/O-doped CN	CH_4	13.83 $\mu mol{\cdot}g^{-1}$ (8 h)	[101]
Ag_1@PCN	CO	0.32 $\mu mol\ h^{-1}$ (2 mg)	[102]
Rh_2/HCNS-Nv	CH_4/CO	14.16/5.16 $\mu mol^{-1}g^{-1}h^{-1}$	[103]
LRSTO/CN	CH_4/CO	1.8/4.1 $\mu mol^{-1}g^{-1}h^{-1}$	[104]
B-doped CN	CO	22.45 $\mu mol^{-1}g^{-1}h^{-1}$	[105]
2D CN@BiOI	CO	458.0 $\mu mol\ h^{-1}m^{-2}$	[106]
CN-MRF	CH_3OH	0.99 $\mu mol\ h^{-1}$ (100 mg)	[107]

3.4. Photocatalytic Synthesis of H_2O_2

Photocatalytic synthesis of H_2O_2 is a green, safe, and sustainable synthesis method that uses solar energy to oxidize and reduce H_2O and O_2 to generate H_2O_2 under mild conditions. Surface modification of CN can greatly improve the efficiency of photocatalytic synthesis of H_2O_2 and, therefore, has attracted great attention from researchers. Chen et al. proposed a hydroxyl-induced CN homojunction strategy that can simultaneously optimize bulk charge separation and suppress surface reverse reactions. Calvin probe tests combined with DFT calculations confirm that the surface hydroxyl groups of CN can provide additional regulatory effects on the migration of electrons from the bulk to the surface. Furthermore, due to the presence of surface hydroxyl groups, the kinetics of the two-electron oxygen reduction reaction (ORR) is more favorable than that of the four-electron ORR, thus the decomposition of H_2O_2 is suppressed. Photocatalytic test results show that the H_2O_2 production of the homojunction sample is increased by 4.5 times compared with the original CN, with an apparent quantum efficiency of 2.1% at 500 nm [108]. He et al. designed a new method to first break CN into smaller fragments (CN-NH_4) and then put them into a directed healing process to create multiple ordered-disordered interfaces (CN-NH_4-NaK). The resulting CN-NH_4-NaK linkages significantly enhance charge dynamics and promote more spatially ordered separated redox centers. The results of photocatalytic studies have shown that CN-NH_4-NaK exhibits good catalytic activity for the synthesis of H_2O_2 via two-step single-electron and one-step two-electron oxygen reduction pathways, with a selectivity of up to 91%, a photochemical conversion efficiency of over 2.3%, and a yield of 16,675 $\mu mol^{-1}g^{-1}h^{-1}$, which is 158 times that of the original CN [109]. Zhou et al. used melamine as raw material to obtain CN hollow tubes (MCN) through hydrothermal self-assembly and calcination and used thiourea as raw material to obtain CN nanosheets (SCN) by calcination. Subsequently, MCN, SCN, and cellulose-based carbon nanofibers (CF) were self-assembled by wet hydrogen bonding in aqueous solution. After high-temperature carbonization treatment, the MCN/SCN/CF composite photocatalyst was successfully synthesized. The introduced CF can serve as an electron transfer agent and energy band regulator of the CN-based photocatalyst, inhibiting the recombination of its photogenerated electron-hole pairs. The results of photocatalytic research show that the photocatalytic H_2O_2 generation performance of pure MCN is only 17.06 $\mu mol^{-1}g^{-1}h^{-1}$ due to the easy recombination of photogenerated electrons and holes. However, the optimized MCN/SCN and MCN/SCN/CF photocatalysts exhibit excellent photocatalytic H_2O_2 performance, which are 55.44 $\mu mol^{-1}g^{-1}h^{-1}$ and 87.36 $\mu mol^{-1}g^{-1}h^{-1}$, respectively, which are about 3.25 times and 5.12 times that of MCN [110]. Similarly, Feng et al. reported a novel nitrate anion intercalation decomposition (NID) strategy to effectively exfoliate BCN into few-layer CN (fl-CN), which can expose internal active sites and accelerate charge separation and transport, thereby improving the photocatalytic efficiency. This method only requires the hydrothermal treatment of BCN in a dilute HNO_3 aqueous solution followed by pyrolysis at different temperatures. The decomposition of nitrate anions not only exfoliates BCN and changes its band structure, but also binds oxygen species to fl-CN, which is beneficial for related chemical processes such as O_2 adsorption. The results of photocatalytic research show that in the photocatalytic preparation of H_2O_2 under visible light irradiation, the H_2O_2 yield of the optimal fl-CN-530 catalyst is 952 $\mu mol^{-1}g^{-1}h^{-1}$, which is 8.8 times that of BCN [111].

Meng et al. used Ba metal atoms to modify CN and effectively improved the efficiency of photocatalytic synthesis of H_2O_2. They developed an ingenious strategy by rationally designing Ba atoms to be injected into planar highly ordered CN nanorods (BI-CN) while improving their planar crystallinity and inducing a highly selective two-electron oxygen reduction reaction ($2e^-$ORR) pathway to produce H_2O_2. As shown in Figure 12A–D, the photocatalytic results show that the optimized BI-CN3 photocatalyst exhibits an excellent H_2O_2 production rate of up to 353 $\mu mol^{-1}g^{-1}h^{-1}$, which is 6.1 times higher than that of the original CN, and has high photocatalytic cycle stability. This is mainly because, after the $BaCl_2$-induced in-plane polymerization process, the prepared Ba embedded in

the in-plane highly ordered CN nanorods show higher photocatalytic H_2O_2 generation activity and cyclic stability. However, when the Ba atoms are poisoned by SO_4^{2-} ions, the H_2O_2 generation rate of the BI-CN3 photocatalyst drops sharply, indicating that the embedded barium atoms play a decisive role in the photocatalytic activity and H_2O_2 generation selectivity. In addition, in the O_2 environment, as the light irradiation time increases, the H_2O_2 production rate is much higher than that in air and Ar environments. Figure 12E presents the schematic process of photocatalytic synthesis of H_2O_2. Experimental and theoretical calculations show that O_2 molecules are efficiently adsorbed on the BI-CN photocatalyst through the Pauling-type configuration. Due to the good in-plane crystallinity of the CN structure, the photoexcited electrons can be effectively separated and rapidly transferred to the electron-deficient Ba active sites, while inducing the end-face adsorbed O_2 molecules to be reduced with H^+ to form *OOH intermediates. The generated *OOH intermediates together with H^+ can be further reduced by photoexcited electrons to generate H_2O_2 molecules, while the process of *OOH dissociating into *O intermediates to generate H_2O is greatly inhibited. Finally, the generated H_2O_2 molecules can be rapidly desorbed from the Ba implanted layer in the highly ordered CN photocatalyst within the plane, while forming Pauling-type adsorption of another O_2 molecule on the Ba center. This highly selective and efficient two-electron oxygen reduction process enables the highly selective synthesis of H_2O_2 in the highly ordered CN photocatalyst with Ba implantation on the surface [112]. Inspired by the light-enzyme coupling catalytic system in chloroplasts, Zhang et al. used polyethyleneimine (PEI) as a "bridge" and loaded Au nanoparticles (AuNPs) as nanozymes on CN nanosheets to prepare a composite catalyst (PEI-GCN/Au). By characterizing the photoelectric properties of the catalyst, it can be found that the introduction of PEI and AuNPs can adjust the electronic structure of CN and promote the rapid separation of photogenerated carriers. The surface plasmon resonance of AuNPs excited by the incident light promotes the activation of glucose molecules and increases their reactivity with O_2, thereby improving the process of GO_X-like catalytic generation of H_2O_2. In addition, DFT calculations show that the grafting of PEI and the addition of glucose enhance the adsorption of O_2 on the catalyst surface and promote the reduction in O_2 to H_2O_2. Therefore, the photocatalytic performance test results show that PEI-GCN/Au can efficiently produce H_2O_2 under visible light with only glucose, H_2O, and O_2 as reactants, and its yield is 270 $\mu mol^{-1}g^{-1}h^{-1}$, which is about 3 times that of ordinary CN photocatalyst [113]. Here, Zhang et al. introduced -C≡N groups and N vacancies (Nv) successively into CN (Nv-C≡N-CN) for the photocatalytic production of high-value chemical H_2O_2 and systematically analyzed the effects of dual defect sites on the entire photocatalytic conversion process. Studies have shown that double defect modification promotes the formation of an electron-rich structure and a more localized charge density distribution in CN, which not only enhances light absorption and carrier separation capabilities but also significantly improves the selectivity and activity of H_2O_2 generation. In addition, experimental characterization and theoretical calculations reveal the key role of each defect site in the photocatalytic H_2O_2 surface reaction process. Nv can effectively adsorb and activate O_2, while the -C≡N group can promote the adsorption of H^+, thereby synergistically promoting the generation of H_2O_2. As a result, the H_2O_2 generation rate of Nv-C≡N-CN reached 3093 $\mu mol^{-1}g^{-1}h^{-1}$, and an apparent quantum efficiency of up to 36.2% at 400 nm is obtained, which far exceeds the previously reported CN-based photocatalysts [114]. Finally, the comparison table of the most active photocatalysts is listed in Table 8.

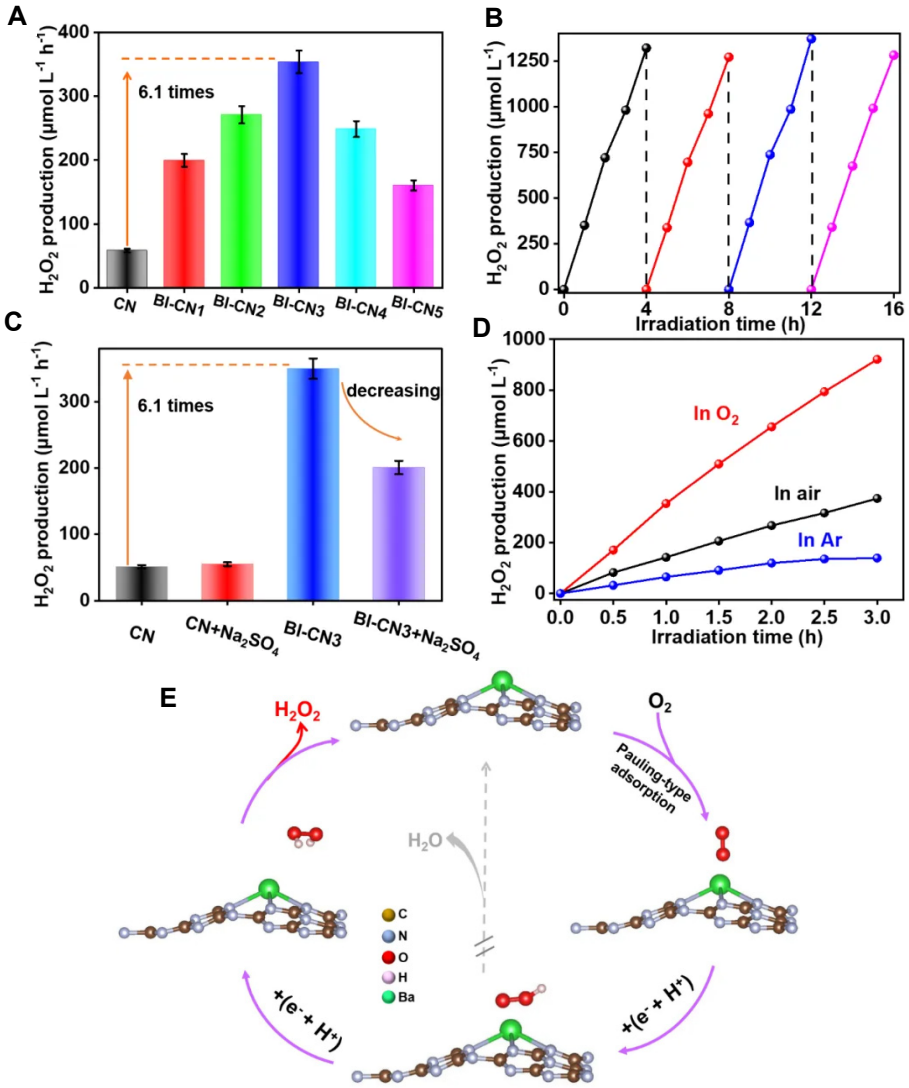

Figure 12. (**A**) Photocatalytic H_2O_2 generation rates of different samples; (**B**) Cyclic H_2O_2 generation test of the BI-CN3 photocatalyst; (**C**) Photocatalytic H_2O_2 activity of bulk CN and BI-CN3 samples in 0.1 mol·L^{-1} Na_2SO_4 solution; (**D**) H_2O_2 evolution activity of BI-CN3 samples under different conditions; (**E**) Mechanism of highly selective photocatalytic synthesis of H_2O_2 via the 2e^-ORR pathway by in-plane highly ordered CN nanorods with Ba implantation [112]. Reprinted with permission from Ref. [112].

Table 8. The photocatalytic activities for H_2O_2 production of CN.

Material Type	Sacrificial Agent	Photocatalytic Performance	Reference
Hydroxyl-rich CN	50 mL ethanol	508 $\mu mol^{-1}g^{-1}h^{-1}$	[108]
CN-NH_4-NaK	10 mL isopropanol/90 mL water	16,675 μmol h^{-1} g^{-1} (30 min)	[109]
MCN/SCN/CF	25 mL distilled water	136.91 $\mu mol^{-1}g^{-1}h^{-1}$	[110]
fl-CN	5 mL ethanol/45 mL water	952 $\mu mol^{-1}g^{-1}h^{-1}$	[111]
BI-CN	4 mL ethanol/36 mL water	353 $\mu mol^{-1}g^{-1}h^{-1}$	[112]
PEI-GCN/Au	10 mL of deionized water	270 $\mu mol^{-1}g^{-1}h^{-1}$	[113]
Nv-C≡N-CN	20 mL pure water	3093 $\mu mol^{-1}g^{-1}h^{-1}$	[114]

4. Summary and Outlook

As a metal-free semiconductor material with unique physicochemical properties and excellent stability, CN has shown broad application prospects in the field of photocatalysis.

In recent years, in order to overcome the problems of a small specific surface area, few active sites, high recombination rate of photogenerated electrons and holes, and narrow visible light absorption range that affect the photocatalytic performance of CN, researchers have implemented various measures to modify CN, including element doping, surface morphology control, defect engineering, heterojunction structure construction, etc. Through these measures, the band structure of CN is adjusted, the surface microstructure of CN is changed, the specific surface area is increased, the transmission distance of photogenerated carriers is shortened, the visible light absorption range is widened, and the recombination of photogenerated electron-hole pairs is effectively suppressed. The modified CN is widely used in photocatalytic degradation of organic pollutants, photocatalytic water splitting to produce hydrogen, photocatalytic reduction in CO_2, and photocatalytic synthesis of H_2O_2, and its photocatalytic performance is greatly improved. However, although current research has made great progress, there are still some problems that need to be solved. For example, the preparation process of surface modification is relatively complicated, the controllability of morphology and structure regulation is poor, the cost of heterojunction construction is high, the internal mechanism of element doping is still not clear enough, and the types of pollutants that can be degraded in the environment are limited. Therefore, future research directions can be considered from the following aspects:

(1) Further improve the visible light absorption range and absorption efficiency of CNby doping with new non-metallic/metallic elements, adjusting the energy band structure of CN, expanding its light response range, and improving its absorption efficiency of visible light. Construct more optimized nanoscale CN structures, such as nanosheets, nanotubes, nanospheres, etc., to increase the specific surface area and improve light capture ability.
(2) Further promote the effective separation of photogenerated electrons and holes in CN. Compound CN with other 0D, 1D, 2D, and semiconductor materials to build a more structurally reasonable composite heterojunction, promote the effective separation of photogenerated electrons and holes, and reduce recombination losses.
(3) Continue to study the photocatalytic mechanism in depth. Through theoretical calculation and experimental verification, in-depth research on the charge transfer, reaction path, and kinetic mechanism in the CN photocatalytic process will be conducted to provide theoretical guidance for the design of new photocatalysts.
(4) In the future, with the continuous innovation of the preparation process, such as nanostructure design and molecular structural engineering, it will be able to prepare CN materials with higher crystallization, larger surface area, and better light absorption performance, and further enhance its light catalytic performance.
(5) Develop efficient and low-cost CN large-scale preparation technology to meet the needs of industrial production. At the same time, combine CN photocatalytic technology with other energy conversion and storage technologies to build an efficient and environmentally friendly energy system.
(6) Expand the types of environmental pollutants that can be degraded by CN photocatalysis. At present, new environmental pollutants such as antibiotics and microplastics are becoming hot topics. Therefore, the application of CN photocatalysts on these pollutants can be gradually expanded to achieve true photocatalytic remediation of environmental pollution.
(7) CN can be introduced in the aspect of new energy conversion area, light energy can be converted into electrical energy or chemical energy, which can be used to prepare high-efficiency solar cells, photocatalytic water decomposition, etc.
(8) For sustainable energy development, in the future, CN can be used to photocatalyze seawater to produce hydrogen, and this is worth researching.

Author Contributions: S.L.: Investigation, Original paper writing. J.T. and J.L. (Jiatong Liu): Investigation, Data correction. Y.L.: Supervision. L.S. and Z.H.: Data correction. J.L. (Jiaming Li): Review and editing. All authors have read and agreed to the published version of the manuscript.

Funding: This work was supported by the Key Area Research and Development Program of Guangdong Province (2020B090922006); National Natural Science Foundation of China (62005081); Guangdong Basic and Applied Basic Research Foundation (2021A1515011932, 2020A1515110985); Science and Technology Program of Guangzhou (202002030165); and the Young Talent Support Project of Guangzhou Association for Science and Technology (QT-2023-007); the Science and Technology Project of Henan Science and Technology Department (232102220014); National Natural Science Foundation of China (12302210).

Data Availability Statement: This paper did not report any data.

Conflicts of Interest: The authors declare no conflict of interest.

References

1. Fujishima, A.; Honda, K. Electrochemical photolysis of water at a semiconductor electrode. *Nature* **1972**, *238*, 37–38. [CrossRef] [PubMed]
2. Fang, Y.; Zheng, Y.; Fang, T.; Chen, Y.; Zhu, Y.; Liang, Q.; Sheng, H.; Li, Z.; Chen, C.; Wang, X. Photocatalysis: An overview of recent developments and technological advancements. *Sci. China Chem.* **2020**, *63*, 149–181. [CrossRef]
3. Kuang, P.; Sayed, M.; Fan, J.; Chen, B.; Yu, J. 3D graphene-based H_2-production photocatalyst and electrocatalyst. *Adv. Energy Mater.* **2020**, *10*, 1903802. [CrossRef]
4. Wang, Z.; Li, C.; Domen, K. Recent developments in heterogeneous photocatalysts for solar-driven overall water splitting. *Chem. Soc. Rev.* **2019**, *48*, 2109–2125. [CrossRef] [PubMed]
5. Marin, M.L.; Santos-Juanes, L.; Arques, A.; Amat, A.M.; Miranda, M.A. Organic photocatalysts for the oxidation of pollutants and model compounds. *Chem. Rev.* **2012**, *112*, 1710–1750. [CrossRef]
6. Yang, C.; Cheng, B.; Xu, J.; Yu, J.; Cao, S. Donor-acceptor-based conjugated polymers for photocatalytic energy conversion. *EnergyChem* **2023**, *6*, 100116. [CrossRef]
7. Wang, L.; Chen, W.; Zhang, D.; Du, Y.; Amal, R.; Qiao, S.; Wu, J.; Yin, Z. Surface strategies for catalytic CO_2 reduction: From two-dimensional materials to nanoclusters to single atoms. *Chem. Soc. Rev.* **2019**, *48*, 5310–5349. [CrossRef]
8. Bie, C.; Zhu, B.; Xu, F.; Zhang, L.; Yu, J. In situ grown monolayer N-doped graphene on CdS hollow spheres with seamless contact for photocatalytic CO_2 reduction. *Adv. Mater.* **2019**, *31*, 1902868. [CrossRef]
9. Li, H.; Song, Q.; Wan, S.; Tung, C.W.; Liu, C.; Pan, Y.; Luo, G.Q.; Chen, H.M.; Cao, S.; Yu, J.; et al. Atomic Interface Engineering of Single-Atom Pt/TiO_2-Ti_3C_2 for Boosting Photocatalytic CO_2 Reduction. *Small* **2023**, *19*, 2301711. [CrossRef]
10. Jang, E.S.; Won, J.H.; Hwang, S.J.; Choy, J.H. Fine tuning of the face orientation of ZnO crystals to optimize their photocatalytic activity. *Adv. Mater.* **2006**, *18*, 3309–3312. [CrossRef]
11. Di, T.; Xu, Q.; Ho, W.K.; Tang, H.; Xiang, Q.J.; Yu, J.G. Review on metal sulphide-based Z-scheme photocatalysts. *ChemCatChem* **2019**, *11*, 1394–1411. [CrossRef]
12. Teter, D.M.; Hemley, R.J. Low-compressibility carbon nitrides. *Science* **1996**, *271*, 53–55. [CrossRef]
13. Wang, X.; Maeda, K.; Thomas, A.; Takanabe, K.; Xin, G.; M-Carlsson, J.; Domen, K.; Antonietti, M. A metal-free polymeric photocatalyst for hydrogen production from water under visible light. *Nat. Mater.* **2009**, *8*, 76–80. [CrossRef] [PubMed]
14. Zheng, Y.; Lin, L.; Wang, B.; Wang, X. Graphitic carbon nitride polymers toward sustainable photoredox catalysis. *Angew. Chem. Int. Ed.* **2015**, *54*, 12868–12884. [CrossRef] [PubMed]
15. Fang, Y.; Wang, X. Photocatalytic CO_2 conversion by polymeric carbon nitrides. *Chem. Commun.* **2018**, *54*, 5674–5687. [CrossRef]
16. Fu, J.; Yu, J.; Jiang, C.; Cheng, B. g-C_3N_4-based heterostructured photocatalysts. *Adv. Energy Mater.* **2018**, *8*, 1701503. [CrossRef]
17. Li, H.; Tao, S.; Wan, S.; Qiu, G.; Long, Q.; Yu, J.; Cao, S. S-scheme heterojunction of ZnCdS nanospheres and dibenzothiophene modified graphite carbon nitride for enhanced H_2 production. *Chin. J. Catal.* **2023**, *46*, 167–176. [CrossRef]
18. Wang, X.; Blechert, S.; Antonietti, M. Polymeric graphitic carbon nitride for heterogeneous photocatalysis. *ACS Catal.* **2012**, *2*, 1596–1606. [CrossRef]
19. Starukh, H.; Praus, P. Doping of graphitic carbon nitride with non-metal elements and its applications in photocatalysis. *Catalysts* **2020**, *10*, 1119. [CrossRef]
20. Yang, Z.; Zhang, Y.; Zhang, H.; Zhao, J.; Shi, H.; Zhang, M.; Yang, H.; Zheng, Z.; Yang, P. Nitrogen vacancies in polymeric carbon nitrides promote CO_2 photoreduction. *J. Catal.* **2022**, *409*, 12–23. [CrossRef]
21. Wang, S.; Zhan, J.; Chen, K.; Ali, A.; Zeng, L.; Zhao, H.; Hu, W.; Zhu, L.; Xu, X. Potassium-doped g-C_3N_4 achieving efficient visible-light-driven CO_2 reduction. *ACS Sustain. Chem. Eng.* **2020**, *8*, 8214–8222. [CrossRef]
22. Zhou, Z.; Zhang, Y.; Shen, Y.; Liu, S.; Zhang, Y. Molecular engineering of polymeric carbon nitride: Advancing applications from photocatalysis to biosensing and more. *Chem. Soc. Rev.* **2018**, *47*, 2298–2321. [CrossRef] [PubMed]
23. Wang, Y.; Phua, S.Z.F.; Dong, G.; Liu, X.; He, B.; Zhai, Q.; Li, Y.; Zheng, C.; Quan, H.; Li, Z.; et al. Structure tuning of polymeric carbon nitride for solar energy conversion: From nano to molecular scale. *Chem* **2019**, *5*, 2775–2813. [CrossRef]
24. Lin, L.; Yu, Z.; Wang, X. Crystalline carbon nitride semiconductors for photocatalytic water splitting. *Angew. Chem. Int. Ed.* **2019**, *131*, 6225–6236. [CrossRef]
25. Savateev, A.; Antonietti, M. Ionic carbon nitrides in solar hydrogen production and organic synthesis: Exciting chemistry and economic advantages. *ChemCatChem* **2019**, *11*, 6166–6176. [CrossRef]

26. Yan, B.; Chen, Z.; Xu, Y. Amorphous and crystalline 2D polymeric carbon nitride nanosheets for photocatalytic hydrogen/oxygen evolution and hydrogen peroxide production. *Chem.-Asian J.* **2020**, *15*, 2329–2340. [CrossRef]
27. Li, H.; Cheng, B.; Xu, J.; Yu, J.; Cao, S. Crystalline carbon nitrides for photocatalysis. *EES Catal.* **2024**, *2*, 411–447. [CrossRef]
28. Yi, J.; El-Alami, W.; Song, Y.; Li, H.; Ajayan, P.M.; Xu, H. Emerging surface strategies on graphitic carbon nitride for solar driven water splitting. *Chem. Eng. J.* **2020**, *382*, 122812. [CrossRef]
29. Shen, R.; Xie, J.; Guo, P.; Che, L.; Chen, X.; Li, X. Bridging the g-C_3N_4 nanosheets and robust CuS cocatalysts by metallic acetylene black interface mediators for active and durable photocatalytic H_2 production. *ACS Appl. Energy Mater.* **2018**, *1*, 2232–2241. [CrossRef]
30. Shi, G.; Yang, L.; Liu, Z.; Chen, X.; Zhou, J.; Yu, Y. Photocatalytic reduction of CO_2 to CO over copper decorated g-C_3N_4 nanosheets with enhanced yield and selectivity. *Appl. Surf. Sci.* **2018**, *427*, 1165–1173. [CrossRef]
31. Wang, L.; Hong, Y.; Liu, E.; Duan, X.; Lin, X.; Shi, J. A bottom-up acidification strategy engineered ultrathin g-C_3N_4 nanosheets towards boosting photocatalytic hydrogen evolution. *Carbon* **2020**, *163*, 234–243. [CrossRef]
32. Mehtab, A.; Ali, S.A.; Ingole, P.P.; Mao, Y.; Alshehri, S.M.; Ahmad, T. MoS_2 nanoflower-deposited g-C_3N_4 nanosheet 2D/2D heterojunction for efficient photo/electrocatalytic hydrogen evolution. *ACS Appl. Energy Mater.* **2023**, *6*, 12003–12012. [CrossRef]
33. Mehtab, A.; Alshehri, S.M.; Ahmad, T. Photocatalytic and photoelectrocatalytic water splitting by porous g-C_3N_4 nanosheets for hydrogen generation. *ACS Appl. Nano Mater.* **2022**, *5*, 12656–12665. [CrossRef]
34. Masih, D.; Ma, Y.; Rohani, S. Graphitic C_3N_4 based noble-metal-free photocatalyst systems: A review. *Appl. Catal. B-Environ. Energy* **2017**, *206*, 556–588. [CrossRef]
35. Yi, J.; Fei, T.; Li, L.; Yu, Q.; Zhang, S.; Song, Y.; Lian, J.; Zhu, X.; Deng, J.; Xu, H.; et al. Large-scale production of ultrathin carbon nitride-based photocatalysts for high-yield hydrogen evolution. *Appl. Catal. B-Environ. Energy* **2021**, *281*, 119475. [CrossRef]
36. Ma, P.; Zhang, X.; Wang, C.; Wang, Z.; Wang, K.; Feng, Y.; Wang, J.; Zhai, Y.; Deng, J.; Wang, L.; et al. Band alignment of homojunction by anchoring CN quantum dots on g-C_3N_4 (0D/2D) enhance photocatalytic hydrogen peroxide evolution. *Appl. Catal. B-Environ. Energy* **2022**, *300*, 120736. [CrossRef]
37. Guo, S.; Deng, Z.; Li, M.; Jiang, B.; Tian, C.; Pan, Q.; Fu, H. Phosphorus-doped carbon nitride tubes with a layered micro-nanostructure for enhanced visible-light photocatalytic hydrogen evolution. *Angew. Chem. Int. Ed.* **2016**, *55*, 1830–1834. [CrossRef]
38. Liu, B.; Ye, L.; Wang, R.; Yang, J.; Zhang, Y.; Guan, R.; Tian, L.; Chen, X. Phosphorus-doped graphitic carbon nitride nanotubes with amino-rich surface for efficient CO_2 capture, enhanced photocatalytic activity, and product selectivity. *ACS Appl. Mater Interf.* **2018**, *10*, 4001–4009. [CrossRef]
39. Li, Y.; Gu, M.; Shi, T.; Cui, W.; Zhang, X.; Dong, F.; Cheng, J.; Fan, J.; Lv, K. Carbon vacancy in C_3N_4 nanotube: Electronic structure, photocatalysis mechanism and highly enhanced activity. *Appl. Catal. B-Environ. Energy* **2020**, *262*, 118281. [CrossRef]
40. Zhang, L.; Ding, N.; Hashimoto, M.; Iwasai, K.; Chikamori, N.; Nakata, K.; Xu, Y.; Shi, J.; Wu, H.; Luo, Y.; et al. Sodium-doped carbon nitride nanotubes for efficient visible light-driven hydrogen production. *Nano Res* **2018**, *11*, 2295–2309. [CrossRef]
41. Guo, L.; Gao, J.; Li, M.; Xie, Y.; Chen, H.; Wang, S.; Li, Z.; Wang, X.; Zhou, W. Synergy of defect engineering and curvature effect for porous graphite carbon nitride nanotubes promoted photocatalytic hydrogen evolution. *EcoEnergy* **2023**, *1*, 437–447. [CrossRef]
42. Preeyanghaa, M.; Vinesh, V.; Neppolian, B. Complete removal of Tetracycline by sonophotocatalysis using ultrasound-assisted hierarchical graphitic carbon nitride nanorods with carbon vacancies. *Chemosphere* **2022**, *287*, 132379. [CrossRef] [PubMed]
43. Zou, R.; Chen, Z.; Zhong, L.; Yang, W.; Li, T.; Gan, J.; Yang, Y.; Chen, Z.; Lai, H.; Li, X.; et al. Nanocellulose-assisted molecularly engineering of nitrogen deficient graphitic carbon nitride for selective biomass photo-oxidation. *Adv. Funct. Mater.* **2023**, *33*, 2301311. [CrossRef]
44. Liang, Y.; Wu, X.; Liu, X.; Li, C.; Liu, S. Recovering solar fuels from photocatalytic CO_2 reduction over W^{6+}-incorporated crystalline g-C_3N_4 nanorods by synergetic modulation of active centers. *Appl. Catal. B-Environ. Energy* **2022**, *304*, 120978. [CrossRef]
45. He, L.; Fei, M.; Chen, J.; Tian, Y.; Jiang, Y.; Huang, Y.; Xu, K.; Hu, J.; Zhao, Z.; Zhang, Q.; et al. Graphitic C_3N_4 quantum dots for next-generation QLED displays. *Mater. Today* **2019**, *22*, 76–84. [CrossRef]
46. Hong, Y.; Yang, J.; Choi, W.M.; Wang, J.; Xu, J. B-doped g-C_3N_4 quantum dots-modified $Ni(OH)_2$ nanoflowers as an efficient and stable electrode for supercapacitors. *ACS Appl. Energy Mater.* **2021**, *4*, 1496–1504. [CrossRef]
47. Dai, X.; Han, Z.; Fan, H.; Ai, S. Sulfur doped carbon nitride quantum dots with efficient fluorescent property and their application for bioimaging. *J. Nanopart. Res.* **2018**, *20*, 315. [CrossRef]
48. Ma, X.; Cheng, H. Self-introduction of carbon nitride quantum dots into carbon nitride planar structure for enhanced photocatalytic hydrogen production. *Appl. Catal. B-Environ. Energy* **2023**, *339*, 123101. [CrossRef]
49. Eroglu, Z.; Sündü, B.; Metin, O. Tailoring the redox ability of carbon nitride quantum dots/reduced graphene oxide-black phosphorus (CNQDs@rGOBP) ternary heterojunctions for photodegradation of organic pollutants. *Mater. Today Sustain.* **2023**, *23*, 100418. [CrossRef]
50. Zhang, Y.; Shen, C.; Lu, X.; Mu, X.; Song, P. Effects of defects in g-C_3N_4 on excited-state charge distribution and transfer: Potential for improved photocatalysis. *Spectrochim. Acta. A* **2020**, *227*, 117687–117714. [CrossRef]
51. Ma, W.; Wang, N.; Guo, Y.; Yang, L.; Lv, M.; Tang, X.; Li, S. Enhanced photoreduction CO_2 activity on g-C_3N_4: By synergistic effect of nitrogen defective-enriched and porous structure, and mechanism insights. *Chem. Eng. J.* **2020**, *388*, 124288. [CrossRef]

52. Lv, C.; Qian, Y.; Yan, C.; Ding, Y.; Liu, Y.; Chen, G.; Yu, G. Defect engineering metal-free polymeric carbon nitride electrocatalyst for effective nitrogen fixation under ambient conditions. *Angew. Chem. Int. Ed.* **2018**, *130*, 10403–10407. [CrossRef]
53. Liu, H.; Ma, S.; Shao, L.; Liu, H.; Gao, Q.; Li, B.; Fu, H.; Fu, S.; Ye, H.; Zhao, F.; et al. Defective engineering in graphitic carbon nitride nanosheet for efficient photocatalytic pathogenic bacteria disinfection. *Appl. Catal. B-Environ. Energy* **2020**, *261*, 118201. [CrossRef]
54. Luo, J.; Liu, Y.; Fan, C.; Tang, L.; Yang, S.; Liu, M.; Wang, M.; Feng, C.; Ouyang, X.; Wang, L.; et al. Direct attack and indirect transfer mechanisms dominated by reactive oxygen species for photocatalytic H_2O_2 production on g-C_3N_4 possessing nitrogen vacancies. *ACS Catal.* **2021**, *11*, 11440–11450. [CrossRef]
55. Shiraishi, Y.; Kofuji, Y.; Sakamoto, H.; Tanaka, S.; Ichikawa, S.; Hirai, T. Effects of surface defects on photocatalytic H_2O_2 production by mesoporous graphitic carbon nitride under visible light irradiation. *ACS Catal.* **2015**, *5*, 3058–3066. [CrossRef]
56. Xie, Y.; Li, Y.; Huang, Z.; Zhang, J.; Jia, X.; Wang, X.; Ye, J. Two types of cooperative nitrogen vacancies in polymeric carbon nitride for efficient solar-driven H_2O_2 evolution. *Appl. Catal. B-Environ. Energy* **2020**, *265*, 118581. [CrossRef]
57. Bao, H.; Wang, L.; Li, G.; Zhou, L.; Xu, Y.; Liu, Z.; Wu, M. Carrier engineering of carbon nitride boosts visible-light photocatalytic hydrogen evolution. *Carbon* **2021**, *179*, 80–88. [CrossRef]
58. Huang, J.; Wang, H.; Yu, H.; Zhang, Q.; Cao, Y.; Peng, F. Oxygen doping in graphitic carbon nitride for enhanced photocatalytic hydrogen evolution. *ChemSusChem* **2020**, *13*, 5041–5049. [CrossRef]
59. Dang, X.; Cui, X.; Zhang, H.; Chen, X.; Zhao, H. Construction of a P, N Co-doped nanocarbon-embedded g-C_3N_4 hollow sphere nanoreactor for the efficient photocatalytic production of hydrogen peroxide. *ACS Sustain. Chem. Eng.* **2023**, *11*, 13096–13107. [CrossRef]
60. Sun, L.; Li, Y.; Feng, W. Gas-phase fluorination of g-C_3N_4 for enhanced photocatalytic hydrogen evolution. *Nanomaterials* **2021**, *12*, 37. [CrossRef]
61. Zhang, T.; Liu, B.; Li, Q.; Niu, X.; Xia, Z.; Qi, L.; Liu, G.; Liu, Y.; Gao, A.; Wang, H. Enhanced scavenger-free photocatalysis-self-Fenton degradation performance over B-doped NVs modified g-C_3N_4 via promoting Fe(II)/Fe(III) cycle. *Sep. Purif. Technol.* **2025**, *353*, 128386. [CrossRef]
62. Wang, R.; Xu, B.; Wang, J.; Wang, X.; Yao, Y. Selective hydrogen-deuterium exchange in graphitic carbon nitrides: Probing the active sites for photocatalytic water splitting by solid-state NMR. *J. Mater. Chem. A* **2021**, *9*, 3985–3994. [CrossRef]
63. Shi, H.; He, Y.; Li, Y.; Luo, P. Unraveling the synergy mechanism between photocatalysis and peroxymonosulfate activation on a Co/Fe bimetal-doped carbon nitride. *ACS Catal.* **2023**, *13*, 8973–8986. [CrossRef]
64. Jiang, J.; Cao, S.; Hu, C.; Chen, C. A comparison study of alkali metal-doped g-C_3N_4 for visible-light photocatalytic hydrogen evolution. *Chin. J. Catal.* **2017**, *38*, 1981–1989. [CrossRef]
65. Ma, T.; Shen, Q.; Zhaoa, B.; Xue, J.; Guan, R.; Liu, X.; Jia, H.; Xu, B. Facile synthesis of Fe-doped g-C_3N_4 for enhanced visible-light photocatalytic activity. *Inorg. Chem. Commun.* **2019**, *107*, 107451. [CrossRef]
66. Xu, Y.; Fan, M.; Yang, W.; Xiao, Y.; Zeng, L.; Wu, X.; Xu, Q.; SU, C.; He, Q. Homogeneous carbon/potassium-incorporation strategy for synthesizing red polymeric carbon nitride capable of near-infrared photocatalytic H_2 production. *Adv. Mater.* **2021**, *33*, 2101455. [CrossRef]
67. Lu, X.; Liu, X.; Chen, X.; Li, X. Engineering MPx (M= Fe, Co or Ni) interface electron transfer channels for boosting photocatalytic H_2 evolution over g-C_3N_4/MoS_2 layered heterojunctions. *Appl. Catal. B-Environ. Energy* **2019**, *252*, 250–259. [CrossRef]
68. Yi, J.; She, X.; Song, Y.; Xu, H.; Zhang, P.; Mo, Z.; Liu, L.; Du, D.; Li, H. A silver on 2D white-C_3N_4 support photocatalyst for mechanistic insights: Synergistic utilization of plasmonic effect for solar hydrogen evolution. *RSC Adv.* **2016**, *6*, 112420–112528. [CrossRef]
69. Zhao, W.; Ma, S.; Yang, G.; Wang, G.; Zhang, L.; Xia, D.; Huang, H.; Cheng, Z.; Xu, J.; Sun, C.; et al. Z-scheme Au decorated carbon nitride/cobalt tetroxide plasmonic heterojunction photocatalytic for catalytic reduction of hexavalent chromium and oxidation of Bisphenol A. *J. Hazard. Mater.* **2021**, *410*, 124539. [CrossRef]
70. Liu, X.; Wang, S.; Yu, W.; Zhang, J.; Fang, S.; Zhang, J.; Qiu, J.; Kong, F.; Duan, X. Single platinum atoms anchored on holy carbon nitride for efficient photodegradation of sulfonylurea herbicide. *Chem. Eng. J.* **2022**, *446*, 137426. [CrossRef]
71. Zeng, Z.; Ye, F.; Deng, S.; Fang, D.; Wang, X.; Bai, Y.; Xiao, H. Accelerated organic pollutants mineralization in interlayer confined single Pt atom photocatalyst for hydrogen recovery. *Chem. Eng. J.* **2022**, *444*, 136561. [CrossRef]
72. Jin, X.; Wang, R.; Zhang, L.; Si, R.; Shen, M.; Wang, M.; Tian, J.; Shi, J. Electron configuration modulation of nickel single atoms for elevated photocatalytic hydrogen evolution. *Angew. Chem. Int. Ed.* **2020**, *132*, 6894–6898. [CrossRef]
73. Yu, F.; Wang, Z.; Zhang, S.; Ye, H.; Kong, K.; Gong, X.; Hua, J.; Tian, H. Molecular engineering of donor-acceptor conjugated polymer/g-C_3N_4 heterostructures for significantly enhanced hydrogen evolution under visible-light irradiation. *Adv. Funct. Mater.* **2018**, *28*, 1804512. [CrossRef]
74. Shi, Y.; Li, L.; Xu, Z.; Sun, H.; Amin, S.; Guo, F.; Shi, W.; Li, Y. Engineering of 2D/3D architectures type II heterojunction with high-crystalline g-C_3N_4 nanosheets on yolk-shell $ZnFe_2O_4$ for enhanced photocatalytic tetracycline degradation. *Mater. Res. Bull.* **2022**, *150*, 111789. [CrossRef]
75. Hou, J.; Wang, H.; Qin, R.; Zhang, Q.; Wu, D.; Hou, Z.; Yang, W.; Hussain, A.; Tahir, M.; Yin, W.; et al. Grinding preparation of 2D/2D g-C_3N_4/BiOCl with oxygen vacancy heterostructure for improved visible-light-driven photocatalysis. *Carbon Res.* **2024**, *3*, 1. [CrossRef]

76. Ahmad, N.; Kuo, C.F.J.; Mustaqeem, M.; Mujahid, M.; Sangili, A.; Huang, C.-C.; Chang, H.-T. Synthesis of novel Type-II $MnNb_2O_6$/g-C_3N_4 Mott-Schottky heterojunction photocatalyst: Excellent photocatalytic performance and degradation mechanism of fluoroquinolone-based antibiotics. *Chemosphere* **2023**, *321*, 138027. [CrossRef]
77. Chen, J.; Xiao, Y.; Wang, N.; Kang, X.; Wang, D.; Wang, C.; Liu, J.; Jiang, Y.; Fu, H. Facile synthesis of a Z-scheme CeO_2/C_3N_4 heterojunction with enhanced charge transfer for CO_2 photoreduction. *Sci. China Mater.* **2023**, *66*, 3165–3175. [CrossRef]
78. Meng, L.; Zhao, C.; Zhang, X.; Guo, R.; Zheng, Y.; Chu, H.; Fu, H.; Wang, P.; Wang, C. Piezo-photocatalytic synergetic for H_2O_2 generation via dual-pathway over Z-scheme ZIF-L/g-C_3N_4 heterojunction. *Nano Energy* **2024**, *128*, 109795. [CrossRef]
79. Sun, L.; Zhang, Z.; Bian, J.; Bai, F.; Su, H.; Li, Z.; Xie, J.; Xu, R.; Sun, J.; Bai, L.; et al. A Z-Scheme heterojunctional photocatalyst engineered with spatially separated dual redox sites for selective CO_2 reduction with water: Insight by in situ μs-transient absorption spectra. *Adv. Mater.* **2023**, *35*, 2300064. [CrossRef]
80. Chen, R.; Ding, S.; Fu, N.; Ren, X. Preparation of a g-C_3N_4/Ag_3PO_4 composite Z-type photocatalyst and photocatalytic degradation of Ofloxacin: Degradation performance, reaction mechanism, degradation pathway and toxicity evaluation. *J. Environ. Chem. Eng.* **2023**, *11*, 109440. [CrossRef]
81. Du, P.; Wei, Y.; Sun, J.; Ying, Z.; Wu, J.; Xu, N. Synthesis of plasmonic Z-scheme g-C_3N_4/$W_{18}O_{49}$ nanocone arrays with enhanced charge separation. *J. Phys. Chem. C* **2021**, *125*, 4205–4210. [CrossRef]
82. Eroglu, Z.; Metin, O. Internal interactions within the complex type-II heterojunction of a graphitic carbon nitride/black phosphorus hybrid decorated with graphene quantum dots: Implications for photooxidation performance. *ACS Appl. Nano Mater.* **2023**, *6*, 7960–7974. [CrossRef]
83. Alemdar, S.; Basak, A.; Metin, O. Exploring the enhanced catalytic activity of Pt nanoparticles generated on the red phosphorus/graphitic carbon nitride binary heterojunctions in the photo-assisted hydrolysis of ammonia borane. *ACS Appl. Mater. Interf.* **2023**, *15*, 48096–48109. [CrossRef] [PubMed]
84. Yin, H.; Fan, T.; Cao, Y.; Li, P.; Yao, X.; Liu, X. Construction of three-dimensional $MgIn_2S_4$ nanoflowers/two-dimensional oxygen-doped g-C_3N_4 nanosheets direct Z-scheme heterojunctions for efficient Cr (VI) reduction: Insight into the role of superoxide radicals. *J. Hazard. Mater.* **2021**, *420*, 126567. [CrossRef] [PubMed]
85. Xu, Y.; Li, W.; Xu, T.; Wang, G.; Huan, W.; Si, C. Straightforward fabrication of lignin-derived carbon-bridged graphitic carbon nitride for improved visible photocatalysis of tetracycline hydrochloride assisted by peroxymonosulfate activation. *Adv. Compos. Hybrid Mater.* **2023**, *6*, 197. [CrossRef]
86. Zeng, Y.; Zhan, X.; Hong, B.; Xia, Y.; Ding, Y.; Cai, T.; Yin, K.; Wang, X.; Yang, L.; Luo, S. Surface atom rearrangement on carbon nitride for enhanced photocatalysis degradation of antibiotics under visible light. *Chem. Eng. J.* **2023**, *452*, 139434. [CrossRef]
87. Zhang, C.; Ouyang, Z.; Yang, Y.; Long, X.; Qin, L.; Wang, W.; Zhou, Y.; Qin, D.; Qin, F.; Lai, C. Molecular engineering of donor-acceptor structured g-C_3N_4 for superior photocatalytic oxytetracycline degradation. *Chem. Eng. J.* **2022**, *448*, 137370. [CrossRef]
88. Kuate, L.J.N.; Chen, Z.; Yan, Y.; Lu, J.; Guo, F.; Wen, H.; Shi, W. Construction of 2D/3D black g-C_3N_4/BiOI S-scheme heterojunction for boosted photothermal-assisted photocatalytic tetracycline degradation in seawater. *Mater. Res. Bull.* **2024**, *175*, 112776. [CrossRef]
89. Ganesan, S.; Kokulnathan, T.; Sumathi, S.; Palaniappan, A. Efficient photocatalytic degradation of textile dye pollutants using thermally exfoliated graphitic carbon nitride (TE-g-C_3N_4). *Sci. Rep.* **2024**, *14*, 2284. [CrossRef]
90. Huang, T.; Chen, J.; Zhang, L.; Khataee, A.; Han, Q.; Liu, X.; Sun, J.; Zhu, J.; Pan, S.; Wang, X.; et al. Precursor-modified strategy to synthesize thin porous amino-rich graphitic carbon nitride with enhanced photocatalytic degradation of RhB and hydrogen evolution performances. *Chin. J. Catal.* **2022**, *43*, 497–506. [CrossRef]
91. Song, P.; Sun, S.; Cui, J.; Zheng, X.; Liang, S. Organic dye-reformed construction of porous-defect g-C_3N_4 nanosheet for improved visible-light-driven photocatalytic activity. *Appl. Surf. Sci.* **2021**, *568*, 150986. [CrossRef]
92. Li, X.; Luo, Q.; Han, L.; Deng, F.; Yang, Y.; Dong, F. Enhanced photocatalytic degradation and H_2 evolution performance of NCDs/S-C_3N_4 S-scheme heterojunction constructed by π-π conjugate self-assembly. *J. Mater. Sci Technol.* **2022**, *114*, 222–232. [CrossRef]
93. Xiong, J.; Li, X.; Huang, J.; Gao, X.; Chen, Z.; Liu, J.; Li, H.; Kang, B.; Yao, W.; Zhu, Y. CN/rGO@ BPQDs high-low junctions with stretching spatial charge separation ability for photocatalytic degradation and H_2O_2 production. *Appl. Catal. B-Environ. Energy* **2020**, *266*, 118602. [CrossRef]
94. Zhang, L.; Ding, N.; Lou, L.; Iwasaki, K.; Wu, H.; Luo, Y.; Li, D.; Nakata, K.; Fujishima, A.; Meng, Q. Localized surface plasmon resonance enhanced photocatalytic hydrogen evolution via Pt@Au NRs/C_3N_4 nanotubes under visible-light irradiation. *Adv. Funct. Mater.* **2019**, *29*, 1806774. [CrossRef]
95. Yan, F.; Wu, Y.; Jiang, L.; Xue, X.; Lv, J.; Lin, L.; Yu, Y.; Zhang, Y.; Yang, F.; Qiu, Y. Design of C_3N_4-based hybrid heterojunctions for enhanced photocatalytic hydrogen production activity. *ChemSusChem* **2020**, *13*, 876–881. [CrossRef]
96. Yang, H.; Sun, S.; Lyu, J.; Yang, Q.; Cui, J. Mechanism insight into triple S-Scheme intermolecular carbon nitride homojunction with robust built-in electric field for highly enhanced photocatalytic hydrogen evolution. *Chem. Eng. J.* **2024**, *481*, 148297. [CrossRef]
97. Wang, H.; Bian, Y.; Hu, J.; Dai, l. Highly crystalline sulfur-doped carbon nitride as photocatalyst for efficient visible-light hydrogen generation. *Appl. Catal. B-Environ. Energy* **2018**, *238*, 592–598. [CrossRef]

98. Wang, C.; Liu, G.; Song, K.; Wang, X.; Wang, H.; Zhao, N.; He, F. Three-dimensional hierarchical porous carbon/graphitic carbon nitride composites for efficient photocatalytic hydrogen production. *ChemCatChem* **2019**, *11*, 6364–6371. [CrossRef]
99. Yang, R.; Shi, H.; Zhao, J.; Zhang, H.; Zhong, M.; Yang, P. Novel asymmetric aggregation strategy to boost charge separation in carbon nitride polymers for high-performance hydrogen photosynthesis. *ACS Catal.* **2024**, *14*, 9607–9617. [CrossRef]
100. Wu, X.; Fan, H.; Wang, W.; Lei, L.; Chang, X.; Ma, L. Multiple ordered porous honeycombed g-C_3N_4 with carbon ring in-plane splicing for outstanding photocatalytic H_2 production. *J. Mater. Chem. A* **2022**, *10*, 17817–17826. [CrossRef]
101. Li, Q.; Wang, S.; Sun, Z.; Tang, Q.; Liu, Y.; Wang, L.; Wang, H.; Wu, Z. Enhanced CH_4 selectivity in CO_2 photocatalytic reduction over carbon quantum dots decorated and oxygen doping g-C_3N_4. *Nano Res.* **2019**, *12*, 2749–2759. [CrossRef]
102. Hu, S.; Qiao, P.; Yi, X.; Lei, Y.; Hu, H.; Ye, J.; Wang, D. Selective photocatalytic reduction of CO_2 to CO mediated by silver single atoms anchored on tubular carbon nitride. *Angew. Chem. Int. Ed.* **2023**, *62*, e202304585. [CrossRef]
103. Ma, X.; Chen, Q.; Han, C.; Zhou, S.; Li, Z.; Liu, J.; Hu, F.; Wang, J.; Wang, N.; Zhu, Y.; et al. Synergistic optimization of morphology and vacancies on diatomic rhodium catalysts dispersed on carbon nitride for efficient photocatalytic reduction of CO_2. *Adv. Funct. Mater.* **2024**, *34*, 2307733. [CrossRef]
104. Wan, S.; Hou, Y.; Wang, W.; Lu, G.; Wang, C.; Tu, R.; Cao, S. Graphitic carbon nitride/La, Rh co-doped $SrTiO_3$ S-scheme heterojunction for photocatalytic CO_2 reduction. *Rare Metal* **2024**, *43*, 1–11. [CrossRef]
105. Hussien, M.K.; Sabbah, A.; Qorbani, M.; Putikam, R.; Kholimatussadiah, S.; Tzou, D.-L.M.; Elsayed, M.H.; Lu, Y.-J.; Wang, Y.-Y.; Lee, X.-H.; et al. Constructing B-N-P bonds in ultrathin holey g-C_3N_4 forregulating the local chemical environment in photocatalytic CO_2 reduction to CO. *Small* **2024**, *20*, 2400724. [CrossRef]
106. Yang, C.; Zhang, Q.; Wang, W.; Cheng, B.; Yu, J.; Cao, S. 2D/2D g-C_3N_4@ BiOI S-scheme heterojunction with gas-liquid-solid triphase interface for highly efficient CO_2 photoreduction. *Sci. China Mater.* **2024**, *67*, 1830–1838. [CrossRef]
107. Ding, J.; Tang, Q.; Fu, Y.; Zhang, Y.; Hu, J.; Li, T.; Zhong, Q.; Fan, M.; Kung, H.H. Core-shell covalently linked graphitic carbon nitride-melamine-resorcinol-formaldehyde microsphere polymers for efficient photocatalytic CO_2 reduction to methanol. *J. Am. Chem. Soc.* **2022**, *144*, 9576–9585. [CrossRef]
108. Chen, Q.; Lu, C.; Ping, B.; Li, G.; Chen, J.; Sun, Z.; Zhang, Y.; Ruan, Q.; Li, T. A hydroxyl-induced carbon nitride homojunction with functional surface for efficient photocatalytic production of H_2O_2. *Appl. Catal. B-Environ. Energy* **2023**, *324*, 122216. [CrossRef]
109. He, F.; Lu, Y.; Wu, Y.; Wang, S.; Zhang, Y.; Dong, P.; Wang, Y.; Zhao, C.; Wang, S.; Zhang, J.; et al. Rejoint of carbon nitride fragments into multi-interfacial order-disorder homojunction for robust photo-driven generation of H_2O_2. *Adv. Mater.* **2024**, *36*, 2307490. [CrossRef]
110. Zhou, J.; Shan, T.; Zhang, F.; Boury, B.; Huang, L.; Yang, Y.; Liao, G.; Xiao, H.; Chen, L. A novel dual-channel carbon nitride homojunction with nanofibrous carbon for significantly boosting photocatalytic hydrogen peroxide production. *Adv. Fiber Mater.* **2024**, *6*, 387–400. [CrossRef]
111. Feng, B.; Liu, Y.; Wan, K.; Zu, S.; Pei, Y.; Zhang, X.; Qiao, M.; Li, H.; Zong, B. Tailored exfoliation of polymeric carbon nitride for photocatalytic H_2O_2 production and CH_4 valorization mediated by O_2 activation. *Angew. Chem. Int. Ed.* **2024**, *63*, e202401884. [CrossRef] [PubMed]
112. Meng, A.; Ma, X.; Wen, D.; Zhong, W.; Zhou, S.; Su, Y. Towards highly-selective H_2O_2 photosynthesis: In-plane highly ordered carbon nitride nanorods with Ba atoms implantation. *Chin. J. Catal.* **2024**, *60*, 231–241. [CrossRef]
113. Zhang, H.; Liu, L.; Zhang, H.; Wan, Y.; Luo, J. Biomimetic-photo-coupled catalysis for boosting H_2O_2 production. *Chem. Eng. J.* **2024**, *483*, 149183. [CrossRef]
114. Zhang, X.; Ma, P.; Wang, C.; Gan, L.; Chen, X.; Zhang, P.; Wang, Y.; Li, H.; Wang, L.; Zhou, X.; et al. Unraveling the dual defect sites in graphite carbon nitride for ultra-high photocatalytic H_2O_2 evolution. *Energy Environ. Sci.* **2022**, *15*, 830–842. [CrossRef]